

**RESEARCH ARTICLE**

10.1029/2020MS002339

**Special Section:**

The Chinese Academy of Sciences Climate and Earth System Models (CAS-FGOALS and CAS-ESM) and Applications

**Key Points:**

- The land surface model of the Chinese Academy of Sciences (CAS-LSM) is developed
- The model considers the effects of lateral flow, water use, nitrogen discharge and river transport, freeze-thaw fronts, and urban planning
- Evaluation of the updated model shows its advances in simulations of ecohydrological responses to human activities

**Supporting Information:**

- Supporting Information S1

**Correspondence to:**

Z. Xie,  
zxi@lasg.iap.ac.cn

**Citation:**

Xie, Z., Wang, L., Wang, Y., Liu, B., Li, R., Xie, J., et al. (2020). Land surface model CAS-LSM: Model description and evaluation. *Journal of Advances in Modeling Earth Systems*, 12, e2020MS002339. <https://doi.org/10.1029/2020MS002339>

Received 16 SEP 2020

Accepted 8 NOV 2020

Accepted article online 17 NOV 2020

## Land Surface Model CAS-LSM: Model Description and Evaluation

Zhenghui Xie<sup>1,2</sup> , Longhuan Wang<sup>1,2</sup>, Yan Wang<sup>1,2</sup>, Bin Liu<sup>1,2</sup>, Ruichao Li<sup>1,2</sup>, Jinbo Xie<sup>1</sup> ,  
Yujin Zeng<sup>3</sup> , Shuang Liu<sup>4</sup>, Junqiang Gao<sup>5</sup>, Si Chen<sup>1,2</sup>, Binghao Jia<sup>1</sup> , and Peihua Qin<sup>1</sup>

<sup>1</sup>State Key Laboratory of Numerical Modeling for Atmospheric Sciences and Geophysical Fluid Dynamics, Institute of Atmospheric Physics, Chinese Academy of Sciences, Beijing, China, <sup>2</sup>College of Earth and Planetary Sciences, University of Chinese Academy of Sciences, Beijing, China, <sup>3</sup>Program in Atmospheric and Oceanic Sciences, Princeton University, Princeton, NJ, USA, <sup>4</sup>Key Laboratory of Mountain Hazards and Earth Surface Processes, Institute of Mountain Hazards and Environment, Chinese Academy of Sciences, Chengdu, China, <sup>5</sup>School of Mathematics and Statistics, Nanjing University of Information Science and Technology, Nanjing, China

**Abstract** Comprehensive land surface models are very important for climate and weather forecasting and for improving our understanding of the relationships between humans and the Earth system. This work presents a land surface model of the Chinese Academy of Sciences (CAS-LSM) that considers groundwater lateral flow, human water regulation, soil freeze-thaw front dynamics, riverine dissolved inorganic nitrogen transport, anthropogenic heat release, urban water usage, and urban planning based on the Community Land Model. Global simulations with the updated CAS-LSM were conducted to evaluate its performance, and the results show its advantages in reproducing ecohydrological processes. Groundwater lateral flow can replenish the groundwater depletion cone caused by overexploitation, where the offset rate increases as the aquifer thickness increases. The maximum thaw depth increases by  $3.62 \text{ mm yr}^{-1}$  in permafrost areas, and the maximum frost depth decreases by  $1.89 \text{ mm yr}^{-1}$  in seasonally frozen areas. Nitrogen fertilizer use and point-source pollution increase the riverine dissolved inorganic nitrogen flow rate in western Europe and eastern China. To further verify the model's ability to simulate the effects of urban planning implementation, simulations over Beijing were conducted using the Weather Research and Forecasting (WRF) model coupled with CAS-LSM. The results show that anthropogenic heat release enhances the sensible heat flux and temperature in the city center. In terms of urban water planning, most of the total water supply in Beijing should be used for urban irrigation, and a small part should be used for road sprinkling to obtain a greater cooling effect.

**Plain Language Summary** This work presents a land surface model of the Chinese Academy of Sciences (CAS-LSM) that considers groundwater lateral flow, human water regulation, soil freeze-thaw front dynamics, riverine dissolved inorganic nitrogen transport, anthropogenic heat release, urban water usage, and urban planning based on the Community Land Model. Global simulations with the updated CAS-LSM were conducted to evaluate its performance, and the results show its advantages in reproducing ecohydrological processes. Simulations conducted using the Weather Research and Forecasting (WRF) model coupled with CAS-LSM over Beijing show that the model can be used for urban water management. The results demonstrate that CAS-LSM is a feasible tool for studying the effects of human activities on land surface processes.

### 1. Introduction

Land surface processes consist of the turbulent transport of momentum, heat, and water between the land's surface, canopy, and the atmospheric boundary layer, as well as thermal and hydrological processes in the soil and snow (Kowalczyk et al., 2013; Niu et al., 2011). These processes are complex and are affected by human activities, solar radiation, and gravity, as well as climate and environmental conditions. Land surface changes have attracted wide attention, especially those caused by human activities, including greenhouse gas emissions, anthropogenic heat emissions, urbanization, and agricultural activities.

Human water use, such as agricultural irrigation, increases the latent heat flux, reduces the sensible heat flux and net ecosystem exchange (Xie et al., 2018; Zeng, Xie, Yu, Liu, Wang, Jia, et al., 2016), and influences precipitation through water vapor transport (Zeng, Xie, & Zou, 2017). A groundwater depression cone caused by

©2020. The Authors.

This is an open access article under the terms of the Creative Commons Attribution-NonCommercial-NoDerivs License, which permits use and distribution in any medium, provided the original work is properly cited, the use is non-commercial and no modifications or adaptations are made.

overexploitation can be replenished through groundwater lateral flow (Zeng, Xie, Yu, Liu, Wang, Jia, et al., 2016), which is closely related to groundwater extraction. Stream water conveyance over riparian banks affects ecological and hydrological processes through groundwater lateral flow (Di et al., 2011; Fan et al., 2013; Zeng, Xie, Yu, Liu, Wang, Zou, et al., 2016). Groundwater lateral flow significantly modifies the equilibrium groundwater table depth pattern around the world (Fan, 2015; Maxwell & Condon, 2016; Zeng et al., 2018).

The processes of soil freezing and thawing affect both soil moisture and temperature, the carbon-nitrogen (CN) cycle, and water exchanges between the land's surface and the atmosphere, as well as human activities, such as engineering construction (Harada et al., 2009; Iwata et al., 2010; Pang et al., 2009; Schuur et al., 2009; Xia et al., 2017). Moreover, the use of nitrogen fertilizers and point-source pollution has increased the amount of riverine dissolved inorganic nitrogen (Liu et al., 2019). Over the past four decades, the level of urbanization worldwide has risen from 39% to 55% (Chen et al., 2014), increasing the likelihood of extreme climate events, including high temperatures, heavy rains, and droughts (Rizvi et al., 2019; Zhao et al., 2018). Moreover, anthropogenic heat release increases the mean climate temperature, producing more frequent extreme heat events, as well as less frequent extreme cold events in city centers. Urban water usage such as irrigation and road sprinkling also affects the air temperature. Understanding these processes and reasonably representing them in land surface models (LSMs) is vital for effective water management, environmental protection, and social development (Tian et al., 2016; Wood et al., 2011; Xie et al., 2016).

LSMs have become more complex and comprehensive due to three decades of development (Dai et al., 2003; Lawrence et al., 2019; Niu et al., 2011). For instance, groundwater table dynamics have been considered explicitly (Liang & Xie, 2003), and groundwater lateral flow schemes have been incorporated into land models (Ji et al., 2017; Maxwell et al., 2015; Zeng, Xie, Yu, Liu, Wang, Jia, et al., 2016, 2018) to better represent the spatial variability of the groundwater table depth. Soil hydrology schemes, which include human water regulation, can be linked with unconfined aquifers (Pokhrel et al., 2015; Zeng, Xie, & Zou, 2017). As an important indicator of climate and the environment, changes in frost and thaw fronts are considered in soil temperature schemes (Gao et al., 2019; Yi et al., 2006). Additionally, to investigate the effects of excess nutrient outflows through rivers from lands to oceans on coastal ecosystems, Liu et al. (2019) developed a global riverine-dissolved inorganic nitrogen transport scheme in an LSM that included human activities, such as fertilizer applications, pollution discharge, and water regulation. Moreover, schemes of urban planning and anthropogenic heat release were implemented in an LSM and coupled with the regional climate model proposed by Liu (2019) to investigate the effects of urban water usage and energy consumption on urban climate.

Despite these efforts, current LSMs do not synchronously describe groundwater lateral flow, human water use, the changes in frost and thaw fronts, dissolved inorganic nitrogen, anthropogenic heat release, urban water usage, and urban planning. Therefore, in this study, we present an LSM of the Chinese Academy of Sciences (CAS-LSM) that includes all of the above processes based on the Community Land Model 4.5 (CLM4.5), which can provide a comprehensive platform for water and energy simulations and is the land component of the Flexible Global Ocean-Atmosphere-Land System (FGOALS) model (Li et al., 2020). Global simulations performed using the updated CAS-LSM are conducted to evaluate its performance. To further verify the model's ability to simulate the effects of urban planning implementation, simulations over Beijing are conducted using the Weather Research and Forecasting (WRF) model coupled with CAS-LSM.

The remainder of this paper is organized as follows. The physical parameterizations of groundwater lateral flow, human water use, frost and thaw fronts, dissolved inorganic nitrogen, anthropogenic heat release, urban water usage, and urban planning are described in section 2, such that potential users can understand the major features of the model. Section 3 describes model simulations to characterize the performance of the model, primarily from hydrology and energy perspectives. Finally, a summary and discussion are provided in section 4.

## 2. Model Development

The physical parameterizations and main characteristics of CAS-LSM are described in this section.

### 2.1. CLM4.5 and CAS-LSM

CLM4.5 is the land surface component of the Community Earth System Model version 1.2 (Gent et al., 2011; Hurrell et al., 2013). CLM 4.5 includes biogeophysical and biogeochemical processes when simulating the

**Table 1**

Comparison Between CLM4.5 and CAS LSM

Module	CLM4.5	CAS LSM	References
BGP	Defined frost table as first frozen layer with unfrozen layer above it Calculated the lateral groundwater flow fluxes by a nonlinear reservoir module and routed it to a river network rather than neighboring grid cells. Included the option to irrigate cropland areas that are equipped for irrigation Fixed anthropogenic heat scheme can be optionally incorporated as modifications to the canyon energy budget	Applied the Stefan equation to calculate frost and thaw fronts The lateral groundwater flow module is based on the Darcy's Law and the Dupuit approximation Including irrigation, and other activities related to industrial and domestic water use Spatiotemporal dynamic anthropogenic heat release data replaces fixed values Included urban planning to determine the optimal urban water usage	Gao et al. (2016), Oleson (2013), and Xie and William (2013) Bear (1972) and Zeng et al. (2018) Zeng et al. (2016) Liu (2019)
BGC	Fixed fertilizer amount for each temperate crop	Used a new gridded nitrogen fertilizer data set to replace the default data.	Liu et al. (2019)
RTM	Routed water from each grid cell to its downstream neighboring grid cell.	Implemented the riverine nitrogen transport with the disturbances from point-source pollution and surface water regulations	Liu et al. (2019)

Note. BGP means biogeophysical processes, and BGC means biogeochemical processes.

water and energy exchanged from the atmosphere to the land surface and exported to the oceans. Biogeophysical processes include momentum, heat and water from the canopy, vegetation and soil, and stomatal physiology and photosynthesis (Lawrence et al., 2011; Oleson, 2013). CAS LSM is the land component of Flexible Global Ocean-Atmosphere-Land System model grid-point version 3 (CAS-FGOALS-g3; Li et al., 2020), which is an extension of CLM4.5. Similar to CLM4.5, CAS LSM uses a subgrid hierarchy with numerous soil columns in each grid cell. Different land units, including vegetation, urban areas, lakes, wetlands, and glaciers, coexist in a grid cell. Land units, soil columns, and plant function types are used to describe the heterogeneity within each grid cell. Building on CLM4.5, CAS LSM couples the groundwater lateral flow, human water use, frost and thaw fronts, dissolved inorganic nitrogen dynamics, anthropogenic heat release, urban water usage, and urban planning as optional configurations, with the target of yielding more complete land surface modeling. Table 1 lists a summary of the changes in CAS LSM relative to CLM4.5. The schematic diagram describing the major processes of CAS LSM is shown in Figure 1. Note that these processes were developed based on CLM4.5. As shown in Figure 2, the content displayed in black font is the original part of CLM4.5, and the content displayed in red font is the new or modified part of this work. Next, the physical parameters and main characteristics of CAS LSM are introduced.

## 2.2. Quasi-Three-Dimensional Groundwater Flow

Soil water flow in an unsaturated zone occurs mainly in the vertical direction due to the effects of gravity, while groundwater flow in a saturated zone can be approximated as a horizontal flow. CAS LSM uses a quasi-three-dimensional model to calculate the groundwater table, that is, a one-dimensional vertical soil water model and a two-dimensional horizontal groundwater model.

For the unsaturated zones, a multilayer model is used to predict soil water content. The soil column is discretized into 15 layers, where the depth of each soil layer,  $z_i$ , is

$$z_i = f_s \{ \exp(0.5(i - 0.5)) - 1 \}, \quad (1)$$

and  $f_s = 0.025$  is a scaling factor.

The Richards equation in one-dimensional form is

$$\frac{\partial \theta}{\partial t} = -\frac{\partial q}{\partial z} - Q, \quad (2)$$

where  $\theta$  is the volumetric soil water content ( $\text{mm}^3 \text{ mm}^{-3}$ ),  $t$  is the time (s),  $z$  is the height in the vertical direction (m), which is positive downward,  $q$  is the soil water flux ( $\text{kg m}^{-2} \text{ s}^{-1}$ ), which is positive upwards,

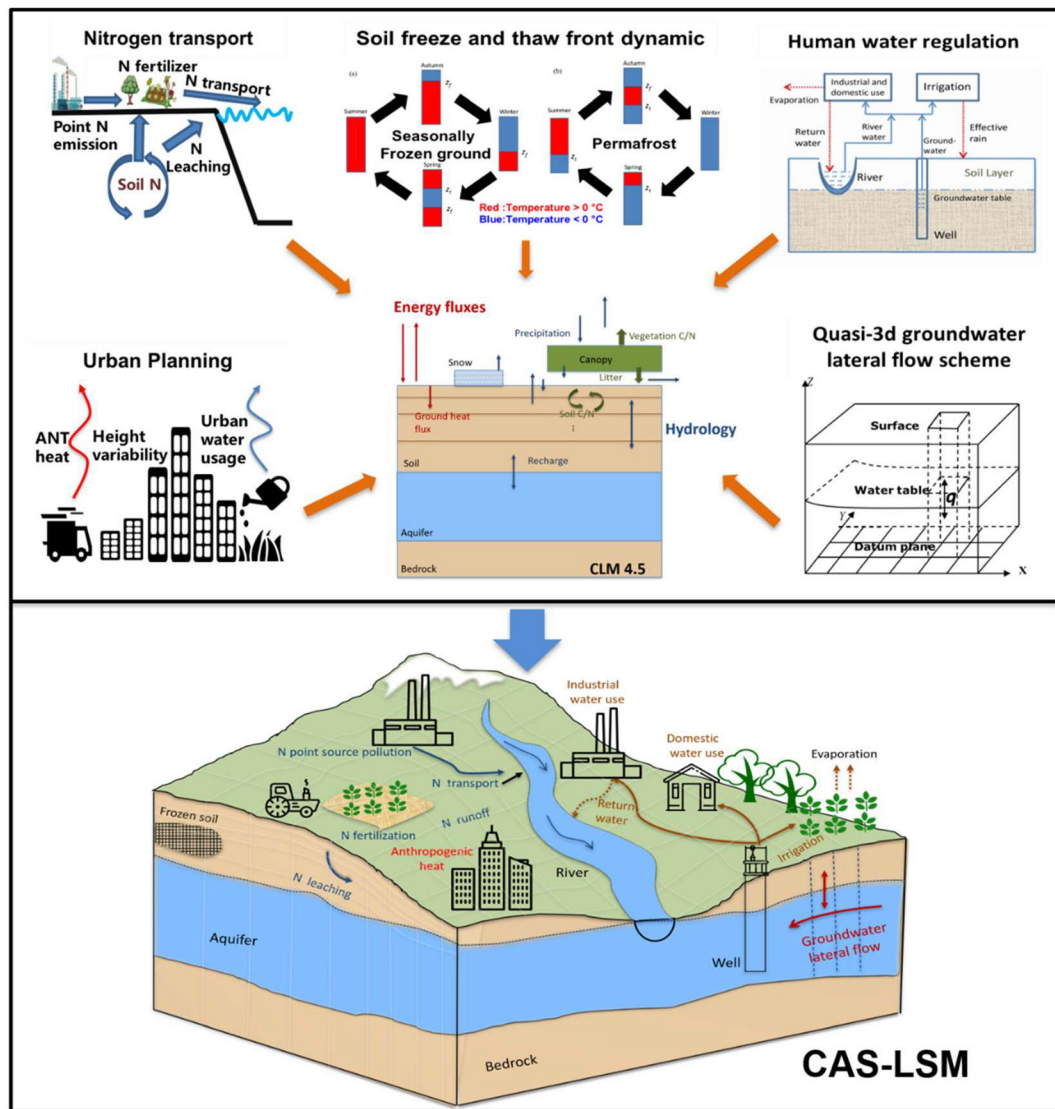


**Figure 1.** The primary processes considered in CAS-LSM, which were developed based on CLM4.5.

and  $Q$  is a soil moisture sink term ( $\text{mm mm}^{-1} \text{s}^{-1}$ ). The solution of Equation 2 is similar to the CLM4.5 (Oleson, 2013).

Groundwater is added as an unconfined aquifer below the soil column, and the vertical groundwater flow is dependent on whether the water table is within or below the soil column. Models that incorporate a scheme that describes groundwater lateral flow can give a more realistic representation of groundwater table depth patterns (Fan et al., 2013; Zeng, Xie, Yu, Liu, Wang, Jia, et al., 2016, 2018). For the saturated zones, the groundwater lateral flow module used in CAS-LSM is based on Darcy's Law and the Dupuit approximation (Bear, 1972) as follows:

$$R = \frac{\partial}{\partial x} \left( T \frac{\partial h}{\partial x} \right) + \frac{\partial}{\partial y} \left( T \frac{\partial h}{\partial y} \right), \quad (3)$$

where  $R$  is the net discharge or recharge rate per unit area ( $\text{m s}^{-1}$ ),  $T$  is the transmissivity ( $\text{m}^2 \text{s}^{-1}$ ),  $h$  is the groundwater table head (m), and  $x$  and  $y$  are the distances in the longitude and latitude directions (m), respectively.

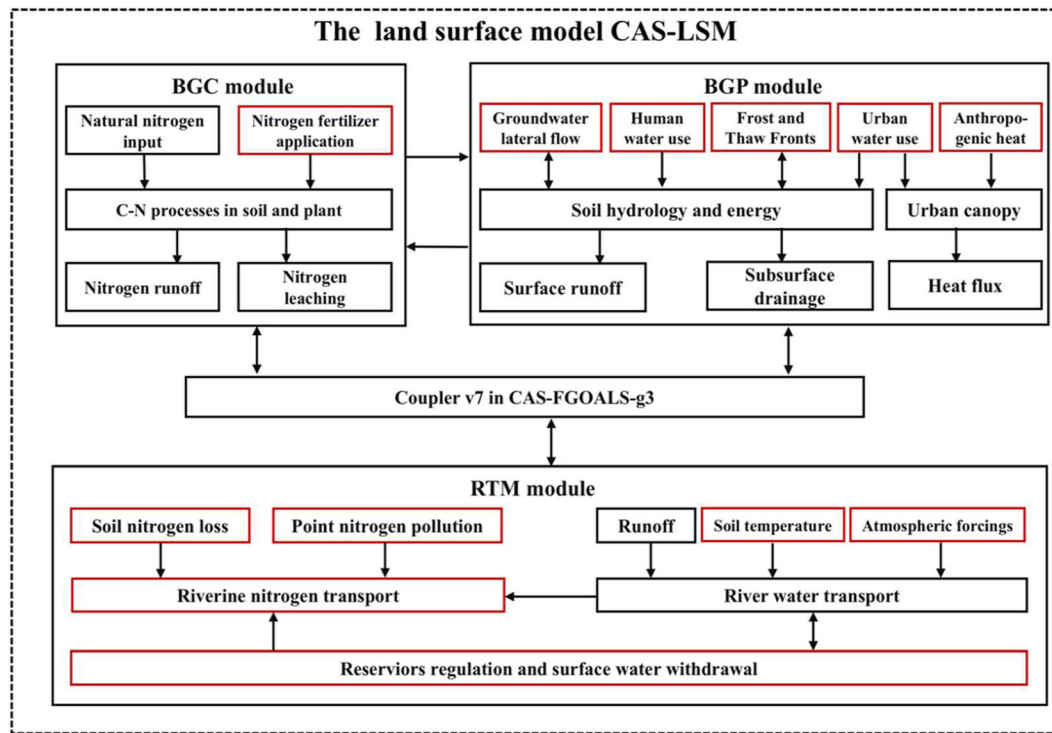


**Figure 2.** Schematic diagram of the CAS-LSM, which considers groundwater lateral flow, human water use, soil freeze-thaw fronts, riverine nitrogen transport, anthropogenic heat release, urban water usage, and urban water planning. The contents shown in black font are the original parts of CLM4.5, while those in red are the newly added or modified parts presented in this work.

After calculating  $R$ , the groundwater table depth,  $d'$ , and the unconfined aquifer water storage,  $W'$ , are written as

$$d' = d - \frac{R \times \Delta t}{s}, \quad (4)$$

$$W' = W + R \times \Delta t, \quad (5)$$

where  $\Delta t$  is the time step (s),  $s$  is the aquifer-specific yield, and  $d$  and  $W$  are the groundwater table depth (m) and unconfined aquifer water storage (m), respectively, before the groundwater lateral flow is calculated.

A reasonable model resolution for running a groundwater lateral flow model is around 1 km (Ji et al., 2017; Xie et al., 2018; Zeng, Xie, Yu, Liu, Wang, Zou, et al., 2016). Note that such a high resolution can cause the calculation of LSMs at the global scale to be very computationally expensive. Thus, CAS-LSM adopts different resolutions in its LSM and groundwater lateral flow model (we ran the LSM at 0.5° resolution and the groundwater lateral flow model at 1-km resolution) based on the conversion scheme of Zeng et al. (2018).

The soil water and groundwater exchange flux,  $q_{recharge}$ , calculated by the CAS-LSM is used as input to the groundwater lateral flow model based on the subgrid structure of CAS-LSM. The value of  $q_{recharge}$  calculated by each plant functional type (PFT) in the 0.5° grid is assigned to the corresponding PFT in the 1-km grid. Smoothing is performed using bilinear interpolation for all 1-km grids. Then, the groundwater lateral flow model calculates the lateral flow and transmits the groundwater lateral flow flux,  $q_{lateral}$ , to the CAS-LSM. From the groundwater lateral flow model to CAS-LSM upscaling, the model accumulates the lateral flux from each 1-km grid in each 0.5° grid, which is divided by the number of grids to find the lateral flux,  $q_{lateral}$ , of the 0.5° grid. Additionally, we use a parallel approach to reduce the calculation time; a detailed description of the parallel running scheme can be found in Zeng et al. (2018).

### 2.3. Human Water Regulation

Human water regulation is classified as groundwater extraction or surface water intake. Groundwater extraction can be represented as pumping water from an aquifer as

$$d'' = d' - \frac{Q_g \times \Delta t}{s}, \quad (6)$$

$$W'' = W' - Q_g \times \Delta t, \quad (7)$$

in which  $Q_g$  is the groundwater pumping rate ( $\text{m s}^{-1}$ ) and  $d''$  and  $W''$  are the groundwater table depth (m) and the water storage of the unconfined aquifer after groundwater use (m), respectively.

Surface water intake can be described as water extraction from rivers as

$$S' = S - Q_s \times \Delta t, \quad (8)$$

where  $Q_s$  is the surface water intake rate ( $\text{m s}^{-1}$ ) and  $S'$  is the surface water stored in the river after subtracting the human water demand (m).

Human water regulation includes agricultural, industrial, and domestic uses. Monthly irrigation data sets (Zeng, Xie, & Zou, 2017) were developed based on the Food and Agriculture Organization (FAO) of the United Nations' global water information system and the Global Map of Irrigation Areas, version 5.0 (GMIA5; Siebert et al., 2005). Industrial and domestic water use are calculated as fractions of the total water consumption for agricultural, industrial, and domestic water use provided by the FAO. Water used for agriculture is visualized as effective rain permeating into the surface soil. Industrial and domestic water use is treated as two sinks, where waste water is treated as runoff, and the net water consumption is treated as evaporation (Zou et al., 2014; Zeng, Xie, & Zou, 2017).

### 2.4. Frost and Thaw Fronts

An assumption in CLM4.5 is that hydrothermal characteristics in the same soil layer are consistent, and a phase transition occurs in the middle of the soil layer, which can lead to delays or advances in soil freezing and thawing simulations (Gao et al., 2019). CAS LSM adopts Stefan's equation (Gao et al., 2019; Jumikis, 1977; Xie et al., 2018) to calculate frost and thaw fronts in a one-directional soil column. Stefan's equation assumes that all the energy absorbed or released during the heat conduction process is used for water freezing or melting. The calculation of frost and thaw fronts can be written as follows:

$$z_f = \sqrt{\frac{2\lambda(T - T_f)t}{L\theta}}, \quad (9)$$

where  $z_f$  is the frost and thaw front depth (m),  $\lambda$  is thermal conductivity ( $\text{W m}^{-1} \text{K}^{-1}$ ),  $T$  is the average soil surface temperature (K),  $T_f$  is the freezing/thawing point temperature (K),  $L$  is the volumetric latent heat of fusion ( $\text{J kg}^{-1}$ ),  $\theta$  is the volumetric fraction of the soil moisture content ( $\text{m}^3 \text{m}^{-3}$ ), and  $t$  is the freezing or thawing duration (s). Equation 9 is calculated at the daily time scale.

To solve Equation 9, we define  $N_i$  as a requirement of the freeze/thaw index for the frost/thaw front to pass from  $z_{i-1}$  to  $z_i$  (Gao et al., 2016, 2019; Xie et al., 2018), where  $z_{i-1}$  is the depth of soil layer  $i$  (m). Here,  $N_i$  can be described as

$$\left\{ \begin{array}{l} N_1 = (L\theta_1 z_1) \left( \frac{R_1}{2} \right), \\ N_2 = (L\theta_2 z_2) \left( R_1 + \frac{R_2}{2} \right), \\ \dots \\ N_i = (L\theta_i z_i) \left( \sum_{n=1}^{i-1} R_n + \frac{R_i}{2} \right), \end{array} \right. \quad (10)$$

where  $\theta_i$  and  $\Delta z_i$  are the volumetric fractions of the soil moisture ( $\text{m}^3 \text{m}^{-3}$ ) and the thickness of soil layer  $i$  (m), respectively, and  $R_i = \Delta z_i / \lambda_i$  is the thermal resistance in soil layer  $i$ .

If the freeze/thaw index  $D = (T - T_f)t$  satisfies  $D \geq \sum_{n=1}^{i-1} N_n$  and  $D < \sum_{n=1}^i N_n$ , then

$$D - \sum_{n=1}^{i-1} N_n = (L\theta_i z_{f0}) (\sum_{n=1}^{i-1} R_n + z_{f0}/2\lambda_i), \quad (11)$$

where  $z_{f0}$  is the frost and thaw front depth for soil layer  $i$ .

Then, we can obtain  $z_{f0}$  as follows

$$z_{f0} = -\lambda_i \sum_{n=1}^{i-1} R_n + \left\{ \lambda_i^2 \left[ \sum_{n=1}^{i-1} R_n \right]^2 + \left[ 2\lambda_i (D - \sum_{n=1}^{i-1} N_n) / (L\theta_i) \right] \right\}^{1/2}, \quad (12)$$

and hence, the frost and thaw fronts depth as

$$z_f = z_{i-1} + z_{f0}. \quad (13)$$

## 2.5. Dissolved Inorganic Nitrogen

A scheme for dissolved inorganic nitrogen was incorporated into CLM4.5 as a submodel by Liu et al. (2019). Dissolved inorganic nitrogen is based on the River Transport Model (RTM), which considers dissolved inorganic nitrogen runoff from soil, as well as leaching, nitrogen deposition, and point-source nitrogen discharge. The RTM routes water from the current grid cell to the grid with the steepest slope in its downstream neighboring grid cells using a linear transport scheme (Graham et al., 1999).

The riverine dissolved inorganic nitrogen outflow flux in each grid cell is calculated as follows:

$$F_{out} = \frac{vS}{d}, \quad (14)$$

where  $v$  is the effective water flow velocity, which is calculated by Manning's formula,  $S$  is the dissolved inorganic nitrogen storage in the grid cell, and  $d$  is the distance between the centers of neighboring grid cells, which is based on the span of the latitude and longitude at the global scale (Oleson, 2013).

The nitrogen balance is as follows:

$$\frac{dS}{dt} = \sum F_{in} - F_{out} + Runoff + Leaching + Pollution + Deposition - Loss, \quad (15)$$

where  $F_{in}$  is the riverine dissolved inorganic nitrogen inflow from eight surrounding grid cells,  $Runoff$  is the dissolved inorganic nitrogen runoff from soil, which is taken away by the surface runoff,  $Leaching$  is the dissolved inorganic nitrogen leached by the soil via subsurface drainage,  $Pollution$  is the point-source nitrogen pollution, which is based on statistics or estimated from data sets,  $Deposition$  is the nitrogen deposited from the atmosphere to rivers, which is ignored as its contribution is very small, and  $Loss$  is the dissolved inorganic nitrogen retention during transport, which is determined by denitrification, sedimentation, and uptake by aquatic plants.

## 2.6. Anthropogenic Heat Release

Anthropogenic heat release is apportioned among vehicles, the building sector, industry, and human metabolism (Sailor & Lu, 2004). These represent the main sources of waste heat in the urban environment, which can be written as

$$AHR = Q_V + Q_B + Q_I + Q_M, \quad (16)$$

where  $Q_V$ ,  $Q_B$ ,  $Q_I$ , and  $Q_M$  are the anthropogenic heat release from vehicles ( $V$ ), the building sector ( $B$ ), industry ( $I$ ), and human metabolism ( $M$ ), respectively. Normally, metabolic heat flux is small in magnitude (less than  $1 \text{ W m}^{-2}$ ) and is almost negligible (Grimmond, 1992; Sailor, 2011). Thus,  $Q_M$  is not considered in the total anthropogenic heat release in this study.

The anthropogenic heat release from vehicles, buildings, and industry can be estimated as follows:

$$AHR = \sum_{i=1}^9 a_i \times E_i, \quad (17)$$

where  $E_i$  represents the  $i$ th kind of energy consumption (where  $i$  can be coal, coke, crude oil, gasoline, kerosene, diesel, fuel oil, natural gas, or electric power) and  $a_i$  represents the heat release coefficient of the  $i$ th kind of energy consumption. The energy consumption is downscaled to the grid cells based on population density; this approach has been commonly used to map total energy consumption to different spatial scales (e.g., Block et al., 2004; Washington, 1972).

## 2.7. Urban Planning and Urban Water Usage

Current urban planning only includes urban water planning, whereas planning in consideration of urban density and energy consumption will be implemented in the future. Here, urban water planning determines the optimal method to reduce the high temperatures in urban areas (to obtain the optimal cooling effect) by allocating water for urban irrigation and road sprinkling. We divide the city into three parts: city center, suburbs, and rural areas according to population density and city type. By simulating the relationship between the water consumption of these three parts of the city, and cooling effects, an optimal water-use scheme can be developed, where the optimal goal is for road sprinkling and urban irrigation to reduce the integrated temperature in these three areas. The optimal water-use scheme can be described as follows:

$$\text{Max: } \sum_{j=1}^3 \sum_{i=1}^2 f_{i,j}(w_{i,j}), \quad (18)$$

where  $i$  represents road sprinkling ( $i = 1$ ) and urban irrigation ( $i = 2$ ),  $j$  represents the three parts of city (city center = 1, suburbs = 2, and rural areas = 3), and  $f_{i,j}(w_{i,j})$  is a function that represents the normalized amount of water use and the associated cooling effects, which can be fitted based on the simulated results.

Considering that the value of the total amount of urban water applied for road sprinkling and urban irrigation is fixed, the water demand of each part of the city should meet the minimum needs of ecology, farmland, plants, roads, and other municipal services. Thus, the constraints for optimizing water use are as follows:

$$\sum_{j=1}^3 \sum_{i=1}^2 w_{i,j} = A, \quad (19)$$

$$b_j \ll w_{1,j} \ll B_j, \quad j = 1, 2, 3, \quad (20)$$

$$c_j \ll w_{2,j} \ll C_j, \quad j = 1, 2, 3, \quad (21)$$

where  $A$  represents the total water supplied for road sprinkling and urban irrigation,  $j$  is defined as above,  $b_j$  and  $B_j$  represent the minimum water demand and the maximum water supply for road sprinkling, respectively, and  $c_j$  and  $C_j$  represent the minimum water demand and the maximum water supply for urban irrigation, respectively. Moreover, additional equalities or inequalities can be added to this optimal water-use planning scheme, and additional water restrictions can be applied in each part of the city.

The simple urban water-use scheme, including urban irrigation and road sprinkling, the road sprinkling scheme was activated in the summer night where water was applied to the impervious layer to accelerate evaporation. The urban irrigation scheme can be described as follows:

$$w_{i,j,t} = \begin{cases} w_{i,j,t}^{\text{ui}}, & \text{pervious layer} \\ a \times \text{pondmax}_{\text{urban}}, & \text{impervious layer}, \\ 0, & \text{otherwise} \end{cases} \quad (22)$$

$$W_{i,j,t} = W_{i,j,t-1} + w_{i,j,t}, \quad (23)$$

$$wo_{i,j,t} = \begin{cases} wo_{i,j,t}^{\text{ui}}, & \text{pervious layer} \\ 0, & \text{otherwise} \end{cases}, \quad (24)$$

$$zwt_{i,j,t} = zwt_{i,j,t-1} - wo_{i,j,t}, \quad (25)$$

where the subscripts  $i,j,t$  represent latitude, longitude, and time, respectively;  $w_{i,j,t}$  represents the total water used for urban irrigation,  $a$  is a coefficient from 0 to 1,  $\text{pondmax}_{\text{urban}}$  represents the maximum

**Table 2**  
*Basic Data*

Data	Resolution	Time periods	Source
CRU forcing	0.5	1901–2010	Viovy (2011)
Bedrock	1 km	—	Shangguan et al. (2017)
Permeability	1 km	—	Gleeson et al., 2011 (2014)
Elevation	1 km	2002	Miliaresis and Argialas, (1999, 2002)
Land cover	1 km	2003	Friedl et al. (2002) and Tateishi et al. (2011)
Groundwater table depth	1 km	Climatological mean	Fan et al. (2013)
Irrigation	0.5	1965–2010	Zeng, Xie, and Zou (2017)
Fertilizer usage	0.5	1961–2013	Liu et al. (2019)
Point-source pollution	0.5	1960–2013	Bouwman et al. (2013) and Morée et al. (2013)
Anthropogenic heat release	3 km	2001–2017	Liu (2019)
Urban water usage	1 km	—	Liu (2019)

water-holding capacity of the urban impervious layer,  $W_{i,j,t}$  and  $W_{i,j,t-1}$  represent the amount of surface liquid water that enters into the first layer soil or the impervious layer at time  $t$  and  $t-1$ , respectively,  $w_{0i,j,t}$  represents the amount of water that is removed from the groundwater, and  $zwt_{i,j,t}$  and  $zwt_{i,j,t-1}$  represent the groundwater table at time  $t$  and  $t-1$ , respectively.

### 3. Simulations

#### 3.1. Data

The basic data sets used for the CAS-LSM simulations are shown in Table 1. The meteorological forcing data, CRUNCEP (Viovy, 2011), which span from 1948 to 2012, have a spatial resolution of  $0.5^\circ$  and a temporal resolution of 3 h. Next, some high-resolution data sets were used in the groundwater lateral flow module. The depth to bedrock was used to constrain the groundwater distribution (Shangguan et al., 2017). The global bedrock permeability and elevation data were obtained from Gleeson et al. (2011, 2014) and the International Steering Committee for Global Mapping (Miliaresis & Argialas, 1999, 2002) to calculate the groundwater lateral flow flux. The global land cover data were obtained from the Global Land Cover by National Mapping Organizations (Friedl et al., 2002; Tateishi et al., 2011), which were used for the resolution conversion. The equilibrium groundwater table depths, which were used as an initial condition before the model was spun-up, were obtained from Fan et al. (2013). We also used the  $0.5^\circ$  monthly irrigation data sets as model input, which were provided by Zeng, Xie, and Zou (2017) and estimated based on the statistical data from FAO. The  $0.5^\circ$  annual fertilizer usage data over croplands were based on statistical data from the International Fertilizer Industry Association and Food and Agricultural Organization (Liu et al., 2019). The point-source pollution data sets were obtained from Morée et al. (2013), which were assumed to directly discharge into rivers (Liu et al., 2019). The anthropogenic heat release data with daily variations only were obtained from Liu et al. (2019), which were based on population density and energy consumption (Block et al., 2004; Washington, 1972). The urban water usage data were obtained from Liu (2019). General information about these data sets is summarized in Table 2.

We collected global and regional data sets to evaluate the capability of CAS-LSM to simulate land surface process, as shown in Table 3. The terrestrial water storages were derived from GRACE satellite data (Rodell et al., 2009; Tapley et al., 2004; Tiwari et al., 2009). The equilibrium groundwater table depth data for ~1.6 million stations around the world were obtained from Fan et al. (2013). The soil moisture product was obtained from the European Space Agency's Climate Change Initiative (ESA-CCI). The global latent heat and sensible heat flux data were sourced from FLUXNET-MTE (Jung et al., 2019; Tramontana et al., 2016). Winter temperatures from 20 sites in Beijing were obtained from the China Meteorological Administration (<http://data.cma.cn/>). The observed dissolved inorganic nitrogen concentrations of 30 large rivers around the world were obtained from the work by Liu et al. (2019).

#### 3.2. Experimental Design

As shown in Table 4, several offline simulations were conducted to assess the impact of the different configurations of the model. Three sets of numerical experiments were completed: (1) the first set of simulations

**Table 3**  
*Validation Data*

Data	Resolution	Time periods	Source
Terrestrial water storage (GRACE satellite data)	1	2002–2010	Rodell et al. (2009), Tapley et al. (2004), and Tiwari et al. (2009)
Groundwater table depth	Site	Climatological mean	Fan et al. (2013)
Soil moisture (ESA-CCI data)	0.25	1979–2010	Dorigo et al. (2017) and Gruber et al. (2017, 2019)
Latent heat flux (FLUXNET-MTE data)	0.5	1982–2010	Jung et al. (2019) and Tramontana et al. (2016)
Sensible heat flux (FLUXNET-MTE data)	0.5	1982–2010	Jung et al. (2019) and Tramontana et al. (2016)
Temperature (Winter temperature in Beijing, China Meteorological Administration)	Site	2010	—
Dissolved inorganic nitrogen concentration	Site	Around 1995	Drecht et al. (2003) and Seitzinger et al. (2005)

included three simulations, EXP1, in which only the frost and thaw fronts module was activated; EXP2, in which the frost and thaw fronts and human water-use modules were activated; and EXP3, in which the frost and thaw fronts, human water use, and groundwater lateral flow modules were activated. EXP1 was used as the baseline simulation in the first set of simulations. (2) A second set of simulations were conducted with the fully prognostic carbon and nitrogen cycle modules accompanied by the crop module. Herein, EXP4 contained the dissolved inorganic nitrogen module, and EXP5 considered fertilizer usage based on EXP4; EXP6 considered point-source pollution based on EXP5.

The first two sets simulations were conducted at the global scale with a horizontal spacing of  $0.5^{\circ}$  for the land and river systems. The time step was 1,800 s for land and 3 h for river transportation. The meteorological forcing data were obtained from the CRUNCEP data set (Vivoy, 2011), which has a 6-h interval and a  $0.5^{\circ}$  horizontal spatial resolution. Note that we spun-up the model for 100 years and 1,000 years for the first and the second sets simulations, respectively, by recycling the meteorological forcing data to reach a quasi-steady state before the formal simulations were performed. The equilibrium groundwater table depth (Fan et al., 2013) was used as an initial condition at 1-km resolution in the groundwater lateral flow module. The evaluation period for the first two sets of simulations was 1991–2010.

To assess the effects of anthropogenic heat release and urban water planning on the urban environment, we also conducted a series of online experiments, which were coupled with the WRF model over Beijing. EXP7 was simulated using the default settings of CLM4.5, while the anthropogenic heat release module was activated for EXP8, and the urban water-use module was activated for EXP10. For the last set simulations, 6-h data (including soil water, moisture, and temperature) from the National Centers for Environmental Prediction (NCEP) Global Final Analysis (FNL) were used for the first-guess initial field and the lateral boundary conditions. Sea-surface temperatures (SSTs) were provided by the NOAA Optimum Interpolation Sea-Surface Temperature (OISST) High-Resolution Dataset (daily frequency,  $0.25^{\circ} \times 0.25^{\circ}$ )

**Table 4**  
*Experimental Design*

Set	Name	Resolution	Period	FTFs	GLF	HWR	DIN	AHR	UWU
1	EXP1	$0.5^{\circ}$	1981–2010	✓	x	x	x	x	x
	EXP2	$0.5^{\circ}$	1981–2010	✓	✓	x	x	x	x
	EXP3	$0.5^{\circ}$	1981–2010	✓	✓	✓	x	x	x
2	EXP4	$0.5^{\circ}$	1991–2010	x	x	x	✓ <sup>a</sup>	x	x
	EXP5	$0.5^{\circ}$	1991–2010	x	x	x	✓ <sup>a</sup>	x	x
	EXP6	$0.5^{\circ}$	1991–2010	x	x	x	✓ <sup>b</sup>	x	x
3	EXP7	3 km	2001–2017	x	x	x	x	x	x
	EXP8	3 km	2001–2017	x	x	x	x	✓	x
	EXP9	1 km	2010	x	x	x	x	x	x
	EXP10	1 km	2010	x	x	x	x	x	✓

Note. FTFs means frost and thaw fronts, GLF means groundwater lateral flow, HWR means human water use, DIN means dissolved inorganic nitrogen, and AHR means anthropogenic heat release. Superscript “a” represents EXP5, in which fertilizer usage was considered based on EXP4. Superscript “b” represents EXP6, in which point-source pollution was considered based on EXP5.

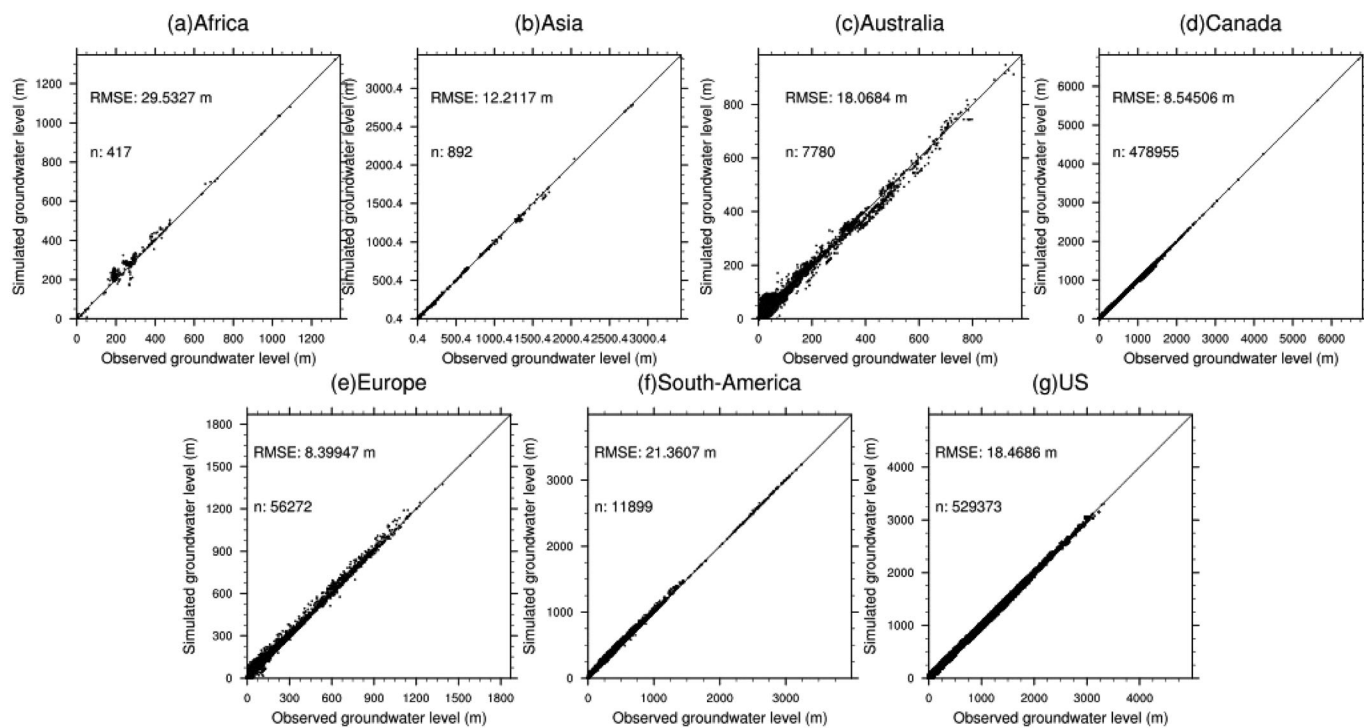


**Figure 3.** Scatter plots for comparing the simulated time-averaged groundwater level from EXP3 with the observed data.

resolution). The default static land-use data provided by USGS were used in the experiments. For the EXP7 and EXP8 simulations, two-layer nested domains with horizontal resolutions of 15 (most of northern China) and 3 km (almost all of the Jing-Jin-Ji metropolitan area, and Beijing) were designed. The simulation period ran from 1 December 1999 to 31 December 2017. The first year, from December 1999 to December 2000, was considered as the initialization period. Results from 2001 to 2017 were used for further analysis. For the EXP9 and EXP10 simulations, three-layer nested domains with horizontal resolutions of 15 (most of northern China), 5 (almost all of the Jing-Jin-Ji metropolitan area,), and 1 km (Beijing) were designed. The summer-time periods from 2000 to 2017 were averaged to 4 days, which represented the climate during May, June, July, and August, where the first day was considered as the spin-up period.

### 3.3. Validation

In this section, we primarily present the simulation results from the perspective of hydrology and energy to characterize the performance of the model. Since multiple modules are involved, the evaluation here is not necessarily complete. For a more in-depth evaluation of the different modules of CAS LSM, please refer to the accompanying manuscript of the CAS-FGOALS Special Issue (Wang, Xie, Xie et al., 2020; Wang, Xie, Jia et al., 2020; Wang, Xie, Liu et al., 2020).

#### 3.3.1. Groundwater Table Depth

Figure 3 displays comparisons between the EXP3-simulated time-averaged groundwater level at 1-km resolution and the observed data in Africa, Asia, Australia, Canada, Europe, South America, and the United States (Fan et al., 2013). Generally, the simulated water levels look satisfactory, and the results from the EXP3 simulations are close to the 1:1 diagonal line. The simulated groundwater levels tend to underestimate the observed data in Africa and South America (Figures 3a and 3f, respectively), while the simulated results in Europe fit better with the observations (i.e., they have a smaller root mean squared errors, RMSEs). The shallower groundwater levels may be related to the limited accuracy of the impermeable bedrock. Figure 3c indicates that the simulated groundwater levels are relatively poor in Australia (with big RMSEs), where has long coastlines. This deficiency is most likely because the boundary conditions have not been considered sufficiently well (here, the sea level was assumed to be 0 m). The above comparison suggests that CAS LSM performs well in producing a reasonable groundwater level.

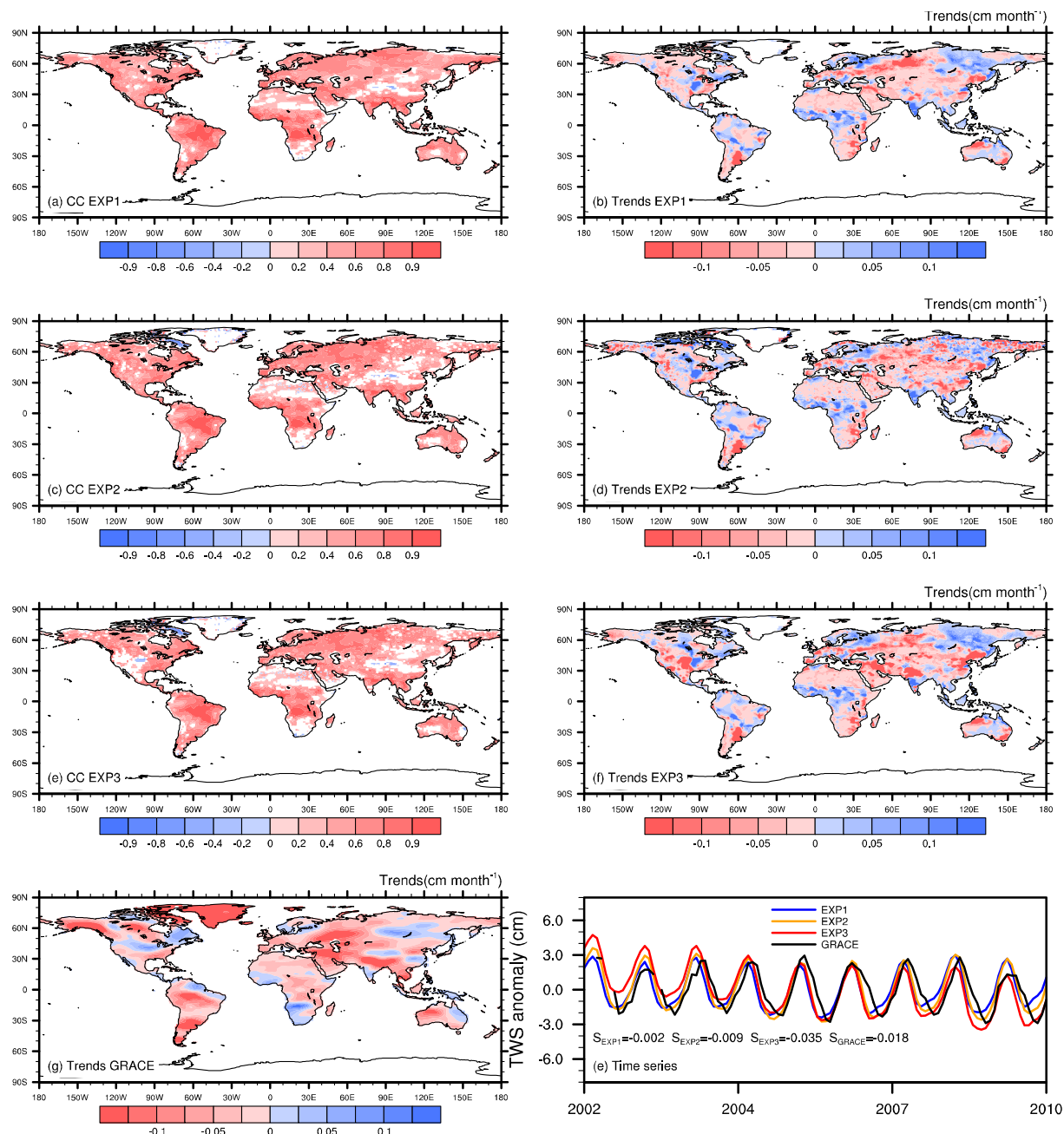


**Figure 4.** (a, c, and e) Correlation between the monthly total water storage time series simulated by EXP1–3 and the GRACE data for the period 2002–2010. The spatial distributions of the TWS linear trends are shown for (b) EXP1-simulated, (d) EXP2-simulated, (f) EXP3-simulated, and (g) GRACE satellite data ( $\text{cm month}^{-1}$ ). (h) Monthly time series of the simulated and observed global-averaged TWSAs.

### 3.3.2. Terrestrial Water Storage

The simulated terrestrial water storage anomalies (TWSAs) were compared with the GRACE satellite data. Figure 4 shows the patterns of the temporal correlation coefficients (CCs) between the monthly TWSAs from the simulations and the GRACE satellite data for 2002–2010, along with their corresponding trends. Overall, both simulations (EXP1 and EXP2) were able to capture the dynamics of the observed TWSAs. Between EXP2 and EXP1 (Figures 4a and 4c, respectively), we found that there is no obvious improvement in the TWSA simulations when considering groundwater lateral flow. As for human water use, a similar conclusion can be found in Figures 4a and 4e, where their CC distributions are not significantly different. This indicates that climate factors play important roles in controlling TWSA variability at the scale of 0.5°. The maps

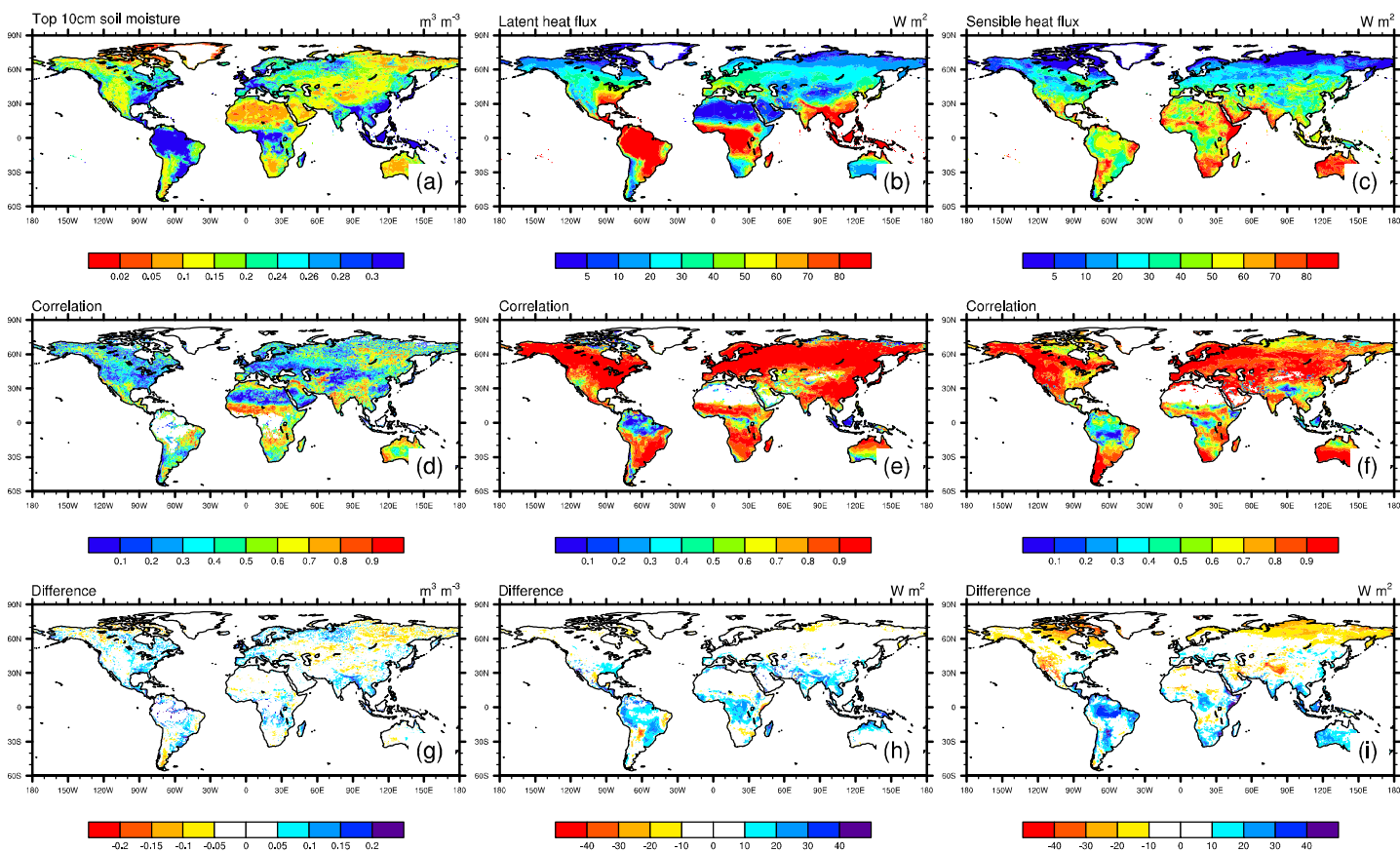


**Figure 5.** Spatial distribution of the climatologic states for (a) top 10-cm soil moisture, (b) latent heat flux, (c) sensible heat flux from the EXP3 simulation, (d) CCs, and (g) differences in spatial patterns of the ESA-CCI soil moistures and the corresponding simulated top 10-cm soil moistures from 1982 to 2010. (e) CCs and (h) the differences in the spatial patterns of the FLUXNET latent heat fluxes and the corresponding simulated latent heat flux from 1982 to 2010. (f) CCs and (i) the differences in the spatial patterns of the FLUXNET sensible heat fluxes and the corresponding simulated values from 1982 to 2010.

of the global trends (Figures 4b, 4d, and 4f) suggest that EXP3 performed reasonably well in overexploited regions (North India and Saudi Arabia). This can be attributed to the human water-use representation in EXP3, which can capture the decreasing trends of TWSA due to groundwater extraction. Figure 4h also illustrates the need to represent human water use in such modeling. The trend of EXP3 is  $-0.035 \text{ cm month}^{-1}$ , which is the closest of the simulated trend of GRACE ( $-0.018 \text{ cm month}^{-1}$ ).

### 3.3.3. Soil Moisture and Energy Flux

Note that the patterns of simulated soil moisture and energy fluxes here are closely related to the biophysical processes of CLM4.5. Since CAS LSM considers new modules based on CLM4.5, we reverified these variables. Figures 5a–5c show the EXP3-simulated global spatial distribution of the climatologic states of the soil moisture, latent heat flux, and sensible heat flux in the top 10 cm of the soil. The presented soil moistures are the weighted averages of the first four soil layer thicknesses (1.75, 2.76, 4.55, and 7.5 cm, with weights of 0.175, 0.276, 0.455, and 0.094, respectively). The soil moistures and latent heat fluxes are similar to the largest values occurring in south and east Asia, eastern North America, western Europe, and the equatorial tropics (Figures 5a and 5b, respectively). Figure 5c shows that the largest values of the sensible heat flux occur in subtropical dry regions, where the available energy is preferentially partitioned to sensible heat flux (Jung et al., 2011).

The spatial distributions of the simulated soil moistures and energy fluxes are seen to be reasonable. Next, we compared the simulated results with the available data products. Figure 5d shows the linear CCs between the ESA-CCI data and the simulated soil moistures from EXP3 for the period 1982–2010. The simulated soil moistures are more accurate in humid regions, such as in India and south Asia. The main differences between the EXP3-simulated results and the ESA-CCI data occur in eastern North America and Europe

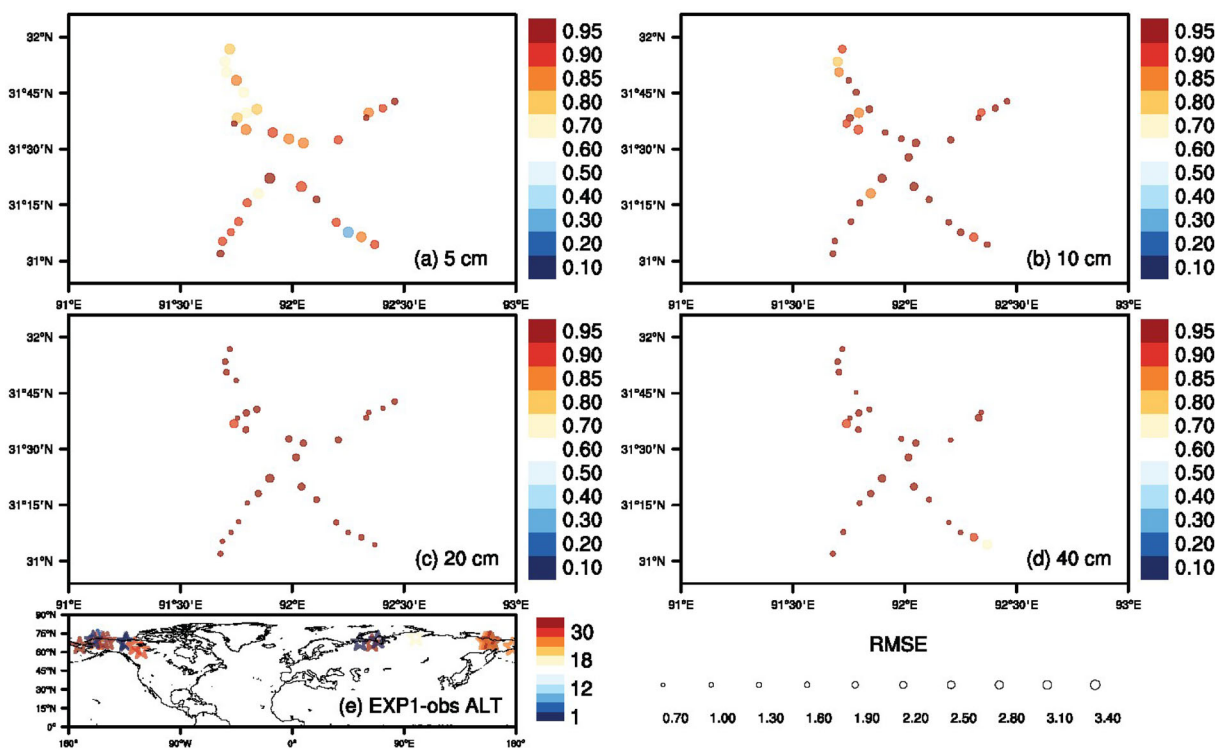


**Figure 6.** (a–d) Soil temperature comparisons between observed and simulated values: CCs and RMSEs ( $^{\circ}\text{C}$ ) between station observations and the EXP1 simulations. The size of the circles corresponds to the magnitude of the RMSE, and the colors represent the values of the CC. (e) RMSEs (cm) between the ALTs from the EXP1 simulation and the 35 sites.

(Figure 5g). This deviation may partly from the meteorological forcing data. The precipitation and air temperature of CRU-NCEP were corrected based on the CRU climatology data rather than observations. Figures 5e and 5f show strong consistency between the FLUXNET data and the simulated energy fluxes (the CCs are higher than 0.8 in most regions), although the simulated energy fluxes are higher than the FLUXNET data in tropical rainforests, such as the Congo Basin and Malaysia.

### 3.3.4. Soil Temperature and Active Layer Thickness

The most important element impacted by frost and thaw fronts is the soil temperature. Figures 6a–6d show the RMSEs and CCs between the daily soil temperatures at 5-, 10-, 20-, and 40-cm depths from the EXP1 simulation and 32 sites from 1 January 2010 to 31 September 2010. The results show that the CAS LSM produces realistic year-long soil temperature profiles, where the RMSEs are  $3.64^{\circ}\text{C}$ ,  $2.39^{\circ}\text{C}$ ,  $1.68^{\circ}\text{C}$ , and  $1.67^{\circ}\text{C}$ , at the aforementioned depths. CAS LSM gives more accurate soil temperatures in deep soil, which is a direct result of the properly simulated positions of the frost and thaw fronts. At greater soil depths, the soil layer is thicker, and the effects of the frost and thaw front position become more pronounced.

The performance of CAS LSM in simulating the depths of soil freezing and thawing in frozen soil regions was validated in previous work (Xie et al. (2018)). In this paper, the distribution of permafrost is calculated based on the simulated frost and thaw fronts depths. If the maximum soil thaw depth in summer is less than the maximum frost depth in winter, the soil is defined as permafrost, and the maximum soil thaw depth is called the active layer thickness (ALT). We compared the simulated ALTs with observations at 35 sites, where Figure 6e shows the RMSEs between the EXP1 simulation and the observations, which show that there is good agreement between them. The RMSEs of the simulated ALTs are 0.24 m. To evaluate the ability of CAS LSM in simulating the distribution of permafrost, we also compared the simulated climatological distribution of permafrost with survey maps (Brown et al., 1997). Figure S1 shows that the simulated permafrost distribution (with a total permafrost area of  $22.1 \times 10^6 \text{ km}^2$ ) is similar to the observed pattern (with an area of  $15.2 \times 10^6 \text{ km}^2$ ) found by Brown et al. (1997). It is also seen that the model underestimates the permafrost extent in the Tibetan Plateau and overestimates the permafrost extent in Russia and Canada.

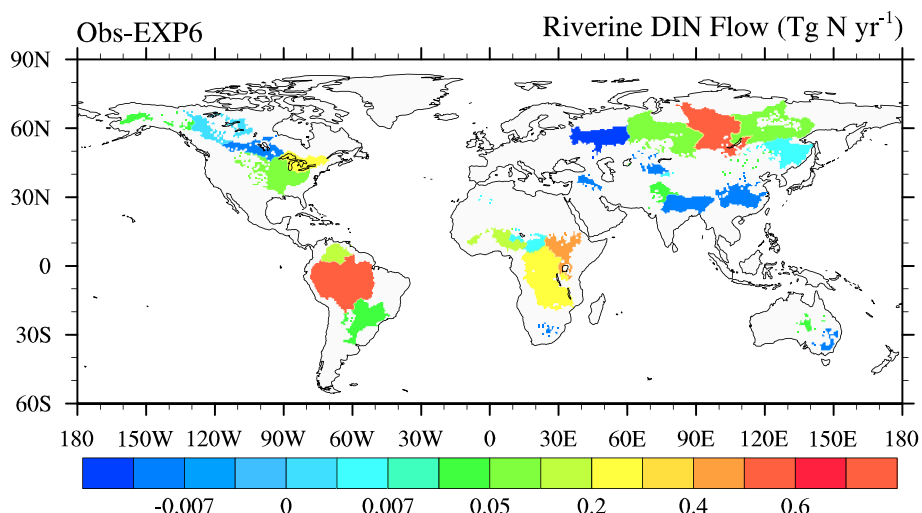


**Figure 7.** Differences in the riverine dissolved inorganic nitrogen flow rates between the EXP6 simulations and observations at 30 large river mouths over the world.

### 3.3.5. Dissolved Inorganic Nitrogen Flow Rate

To check the reasonability of the simulated dissolved inorganic nitrogen flow rate, we compared observed dissolved inorganic nitrogen flow rates with the simulated values obtained from EXP6 at 30 large river mouths across the world in 1995 (Figure 7). The rivers have been ordered in size from the largest to the smallest river basin. The colors represent the annual dissolved inorganic nitrogen flow rate of each individual river. Figure 7 indicates that the CAS LSM underestimates the riverine dissolved inorganic nitrogen flow rates in most river basins, such as the Amazon, Ob, Yenisei, etc. However, the simulated results have the same order of magnitude as the observations, and the CC is 0.56. Consequently, we considered that the model could reproduce the dissolved inorganic nitrogen flow rates for selected rivers with reasonable accuracy in terms of global large-scale modeling. In general, the validations of this study supplement the findings of previous experiments (Zeng, Xie, Yu, Liu, Wang, Jia, et al., 2016; Zeng, Xie, Yu, Liu, Wang, Zou, et al., 2016; Zeng, Xie, & Liu, 2017), demonstrating the ability of CAS LSM to simulate dissolved inorganic nitrogen flow rates.

### 3.3.6. Temperature

A comparison of the daily temperatures from the China Meteorological Administration Land Data Assimilation System (CLDAS) data set with the simulated anthropogenic heat release results is shown in Figure 8. It can be seen that the similar spatial distributions demonstrate that the anthropogenic heat release scheme is reasonable. The CCs between the CLDAS temperatures and the anthropogenic heat release results are primarily close to one, and the average RMSE of the two data sets is  $2.8^\circ\text{C}$ . The gridded model results were interpolated to the CLDAS sites according to the coordinates of the monitoring stations in both urban and suburban areas, where there were nine stations on six ring roads and 11 stations in the suburbs. The comparison between the site observations and the EXP7 and EXP8 simulation results also show that they are in good agreement (Figure 8b). Overall, the results show that the anthropogenic heat release simulation results are reasonable, where the simulated temperatures are slightly higher than observations, with RMSEs less than  $2.5^\circ\text{C}$ . Compared with the automatic weather stations, the absolute errors and RMSEs are relatively small, which shows that the simulated temperatures have good agreement with both the CLDAS data and the station observations.

## 3.4. Impact of Human Activities on Hydrological and Ecological Processes

### 3.4.1. Impact of Human Water Use on the Groundwater Lateral Flow

Excessive groundwater extraction can cause a lower local groundwater level than the surrounding area, which could cause a groundwater depression cone. However, under the effects of a hydraulic gradient, groundwater in the surrounding area could replenish the overextracted area, slowing down the decrease in the groundwater level. Therefore, we further studied the effects of human water use on the

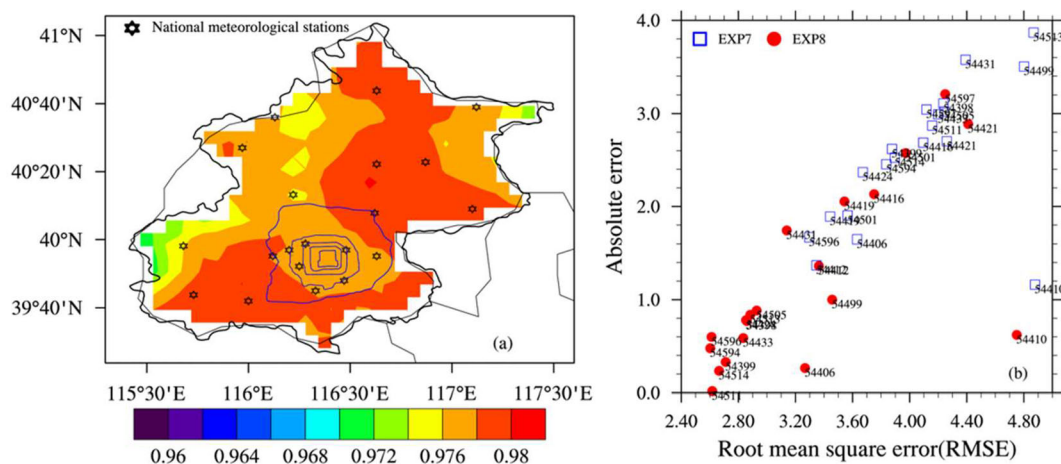


**Figure 8.** Comparison with CLDAS and site data. (a) CCs between the daily temperatures from CLDAS and the EXP8 simulation. (b) RMSEs and absolute error of the winter daily temperatures between 20 national stations and the simulations.

groundwater lateral flow at the global scale. Figure 9 shows the multiyear (1980–2010) mean spatial distributions of “EXP3–EXP2” of the lateral flow flux at 1-km resolution. The results show that the contiguous areas with significant increases in the lateral flow flux are located in northern India, the northern Chinese plains, and the central United States. The groundwater lateral flow fluxes increase by  $100 \text{ mm yr}^{-1}$ .

However, the relationship between the change of groundwater lateral flow and the amount of groundwater extraction is not significantly linear. Even in overexploited areas, any changes of the groundwater lateral flow can be small. For example, Zeng, Xie, Yu, Liu, Wang, Zou, et al. (2016) indicated that terrain slope is a key factor that determines the groundwater lateral flow offset in an extracted area. At the same time, a steep (large terrain slope) area generally has a thin aquifer, which means that recharge from surrounding aquifers will be small due to low water transmissivity. Thus, we further explored the relationship between groundwater lateral flow and aquifer thickness. As shown in Figure S2a, a significant relationship appears only when the groundwater extraction exceeds  $300 \text{ mm yr}^{-1}$ . With an increase of the aquifer thickness, the replenishment effect of the groundwater lateral flow also increases. When the aquifer thickness is greater than 7 m, the replenishment effect of the groundwater lateral flow is basically stable. To better combine the replenishment effects of the groundwater lateral flow with water management, we further explored the relationship between the offset rate (i.e., the ratio of the change of groundwater lateral flow to the amount of groundwater extraction) and aquifer thickness (Figure S2b). We found that the offset rate increased as the aquifer thickness increased and could be as high as 40%. Thus, a relatively high offset rate

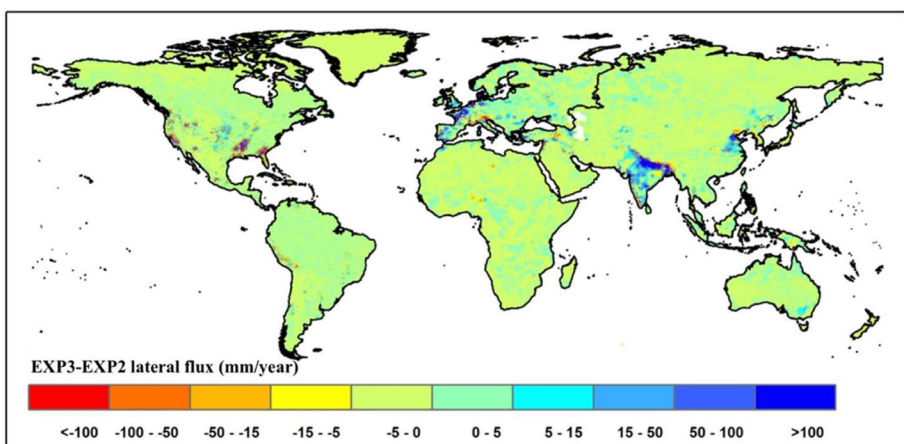


**Figure 9.** Differences in the lateral flow fluxes from EXP3 and EXP2.

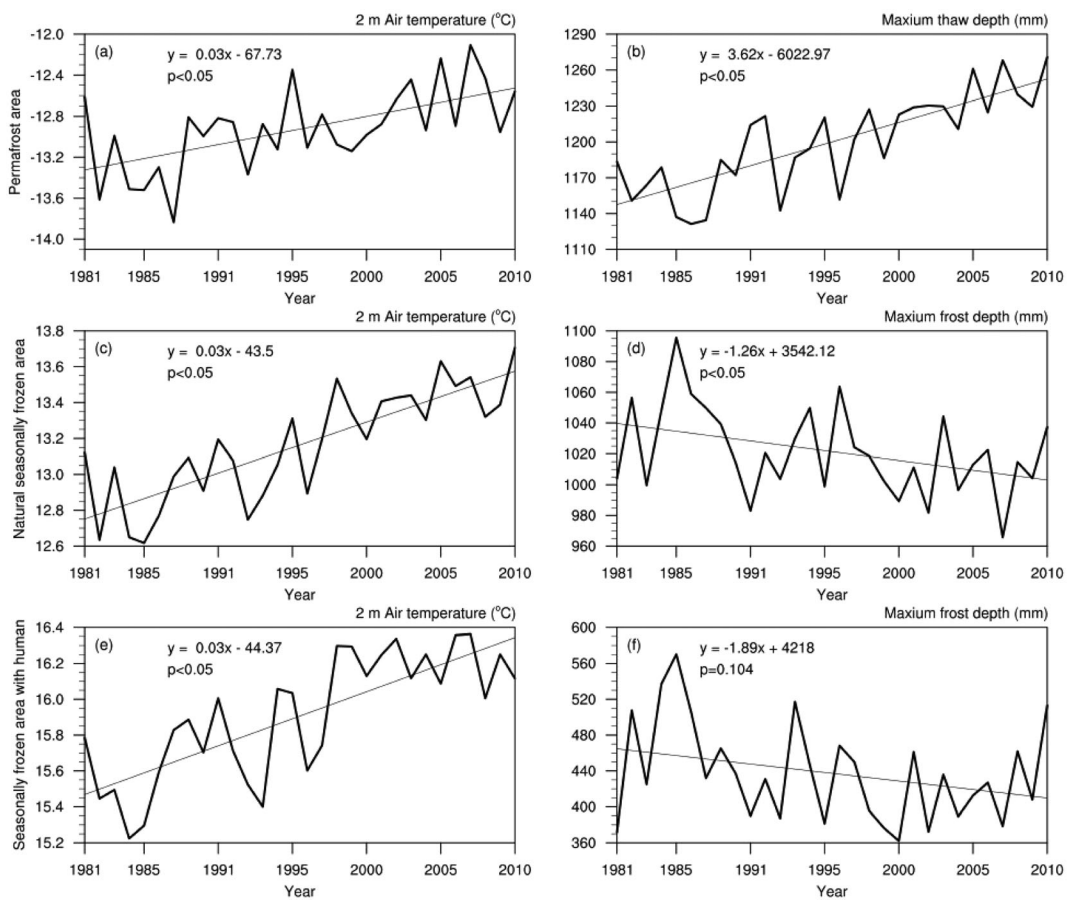


**Figure 10.** (a and b) Interannual variations of the frozen soil in permafrost areas, (c and d) natural areas of seasonally frozen soil, and (e and f) human-dominated areas, from 1981 to 2012 (simulated results from EXP3).

can be obtained by extraction from thick aquifers, which can be used as a reference for the sustainable development of water resources.

#### 3.4.2. Temporal-Spatial Variations of the Frost and Thaw Fronts

Previous studies have indicated that human water use can hamper soil-freezing processes (Xie et al., 2018; Zeng, Xie, Yu, Liu, Wang, Zou et al., 2016). We compared the trends of the spatially averaged annual frost and thaw fronts in permafrost areas, seasonally frozen soil areas, and areas dominated by human activities. Figure 10a shows that the ground temperature in each area rose from 1981 to 2010 at an almost identical rate of  $0.03^{\circ}\text{C yr}^{-1}$ . Figure 10b shows the maximum thaw depth increased at the rate of  $3.62 \text{ mm yr}^{-1}$  in permafrost areas. The shallowest thaw front occurred in 1986, and the deepest occurred in 2010. Regions with degrading permafrost always coincided with a statistically significant increasing temperature (Figures 11d and 11f). Figure 10d indicates that the maximum frost depth decreased at a rate of  $1.26 \text{ mm yr}^{-1}$  in seasonally frozen soil areas that were not dominated by human activities. Figure 11c shows that the maximum frost depth increased slightly in small areas of the seasonally frozen soil and decreased significantly in most areas of the seasonally frozen soil, so that the spatially averaged frost depth appeared to decrease (Figure 10d). Figure 10f shows that the maximum frost depths decreased at a rate of  $1.89 \text{ mm yr}^{-1}$  in human-dominated areas, where the shallowest frost front occurred in 2000, and the deepest occurred in 1985. These changes may support the belief that human water use can hamper the soil-freezing process. Indeed, the effects of human water use on changes of the maximum frost depths are not significant, even in a typical water-consumption area, such as central United States. Figures 11c and 11d indicate that the changes in the soil thaw front in permafrost areas were larger those in areas of seasonally frozen soil. In general, we find that global warming dominates the degradation of permafrost, while human water use only slightly hampers the soil-freezing process.

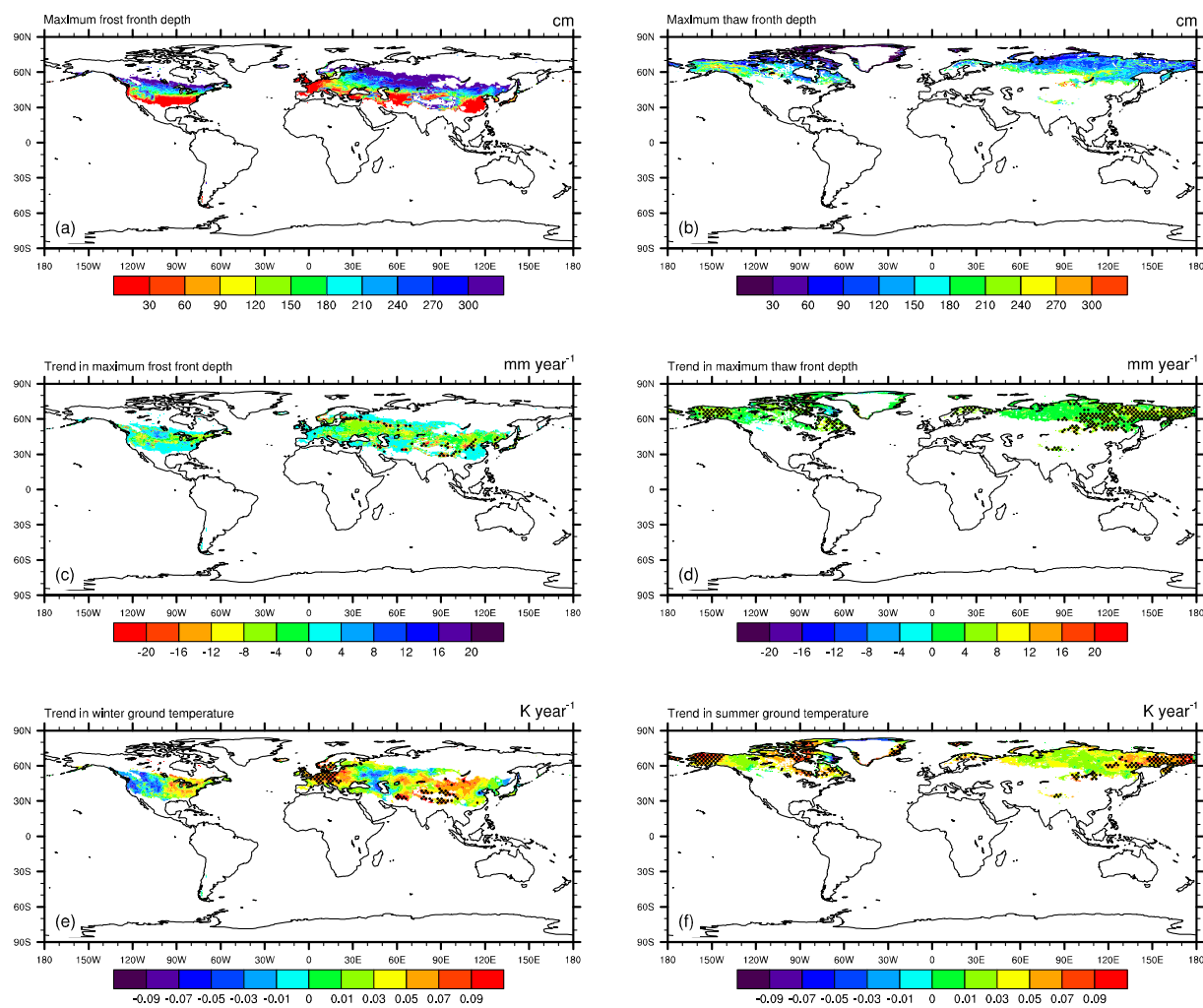


**Figure 11.** Spatial distribution of the climatologic states for (a) maximum frost front depths and (b) maximum thaw front depths. Near 30-year trends of the (c) maximum frost front depths, (d) maximum thaw front depths, (e) ground temperature in winter, and (e) ground temperature in summer.

### 3.4.3. Impact of Anthropogenic Nitrogen Discharge on the Riverine Nitrogen Transport

Figure 12 shows the 20-year averaged spatial distributions of the differences in the riverine-dissolved inorganic nitrogen flow rates across the world between different simulations. Figure 12a displays the contributions of nitrogen fertilizer application to the dissolved inorganic nitrogen in rivers. We find that nitrogen fertilizer applications increased the riverine-dissolved inorganic nitrogen flow rates, especially in the central United States (the Mississippi River), western Europe, and northern China (the Yellow River and the Yangtze River). The annual flow rates increased by about 20,000–40,000 tons. Figure 12b indicates that point-source nitrogen pollution increased the riverine-dissolved inorganic nitrogen flow rates. Almost all the large rivers in the world were affected by widespread human activities. The rivers in western Europe and eastern China were the most polluted, where the annual dissolved inorganic nitrogen increased by 5,000–15,000 tons. Figure 12c displays the combined effects of temperate fertilizer application and point-source nitrogen pollution, which reflects the notion that anthropogenic nitrogen discharge could directly and markedly augment the amount of dissolved inorganic nitrogen in most rivers across the world and is hence an important factor related to riverine environmental problems. Generally, the Mississippi River Basin, the Yellow River Basin, the Yangtze River Basin, and western Europe are the most polluted regions.

### 3.4.4. Impact of Anthropogenic Heat Release on the Urban Energy Flux

Due to the increase of anthropogenic heat release in cities, surface heat fluxes have correspondingly increased. The sensible heat flux, surface temperature and the 2-m air temperature of the entire city of

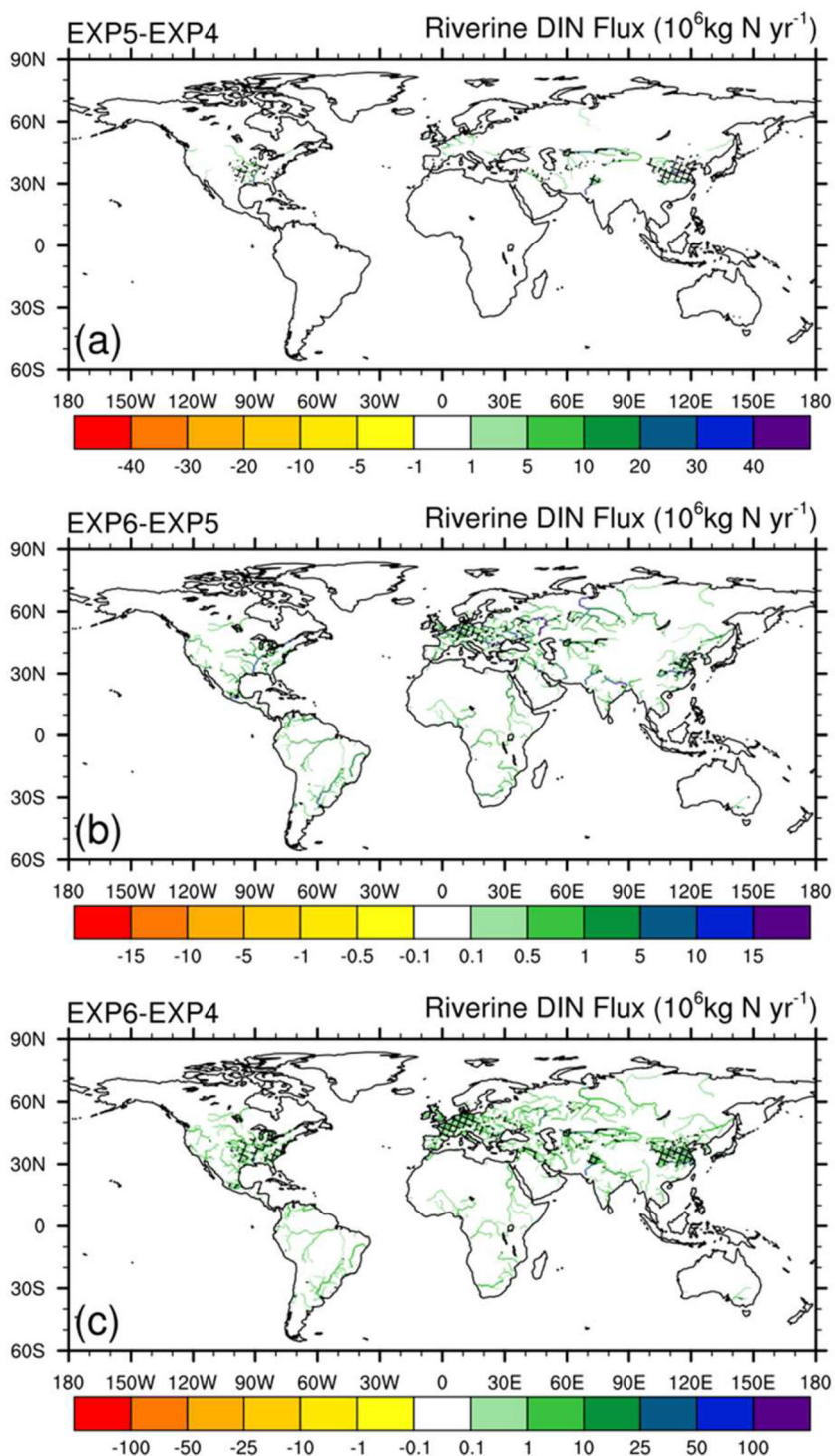


**Figure 12.** Twenty-year averaged spatial distributions of the differences in the riverine dissolved inorganic nitrogen flow rates between different experiments: (a) EXP4 and EXP5, (b) EXP5 and EXP6, and (c) EXP6 and EXP4. This figure demonstrates the effects of temperate fertilizer application, point-source pollution, and their combined effect on the anthropogenic nitrogen discharge and the riverine dissolved inorganic nitrogen flow rates. The black dots indicate regions where the difference passed the 95% confidence level of the Student's *t* test.

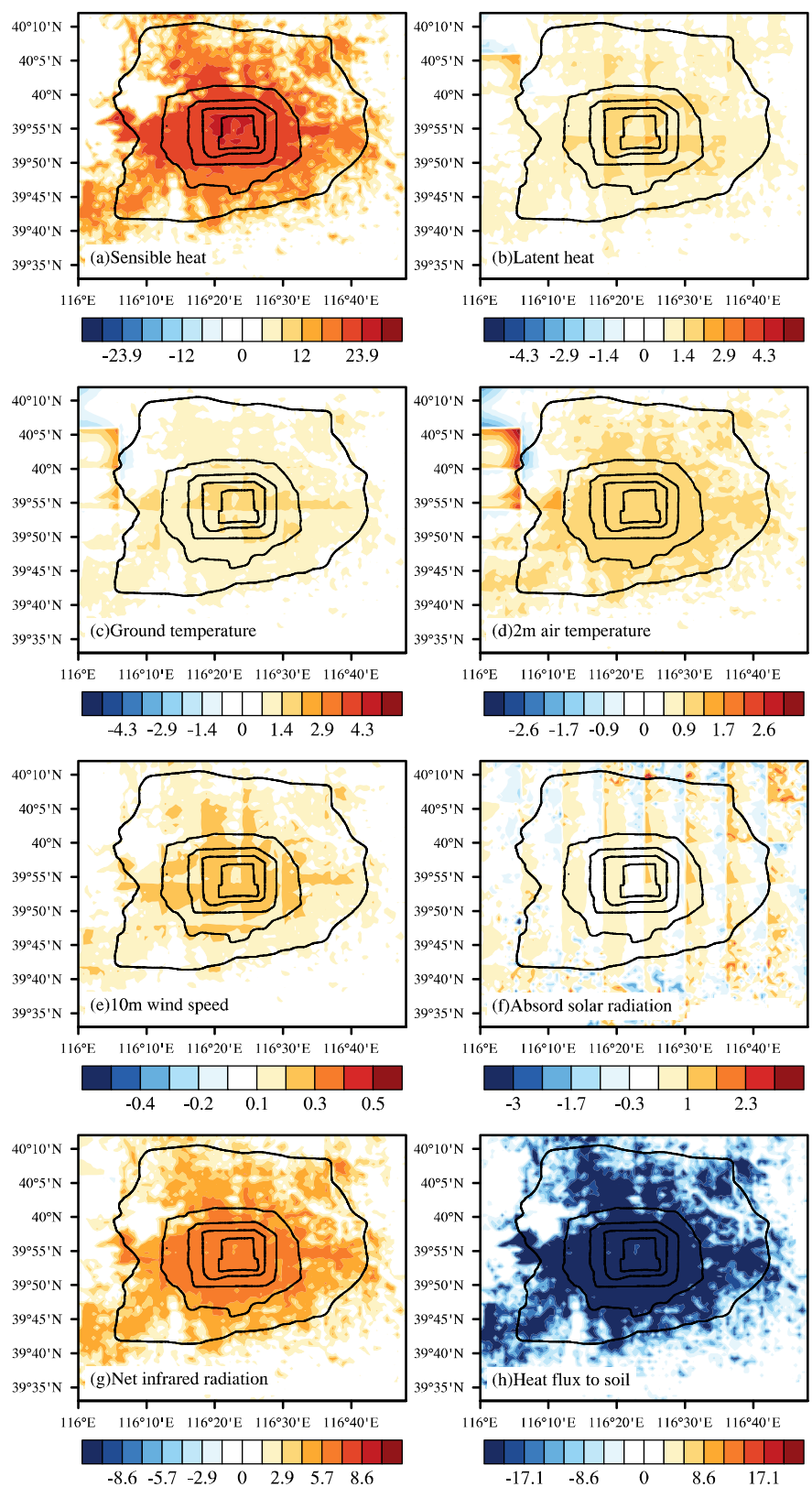


**Figure 13.** Differences of the spatial patterns predicted by the EXP7 and EXP8 simulations of climatological (a) sensible heat, (b) latent heat, (c) ground temperature, (d) 2-m air temperature, (e) 10-m wind speed, (f) absorbed solar radiation, (g) net infrared radiation, and (h) heat flux to the soil.

**Table 5***Relationships Between the Quantities of Water Applied and Their Cooling Effects*

	Road sprinkling	Urban irrigation
City center	$f = 0.15 * w^2 - 0.32 * w - 0.39$	$f = -0.18 * w^2 + 0.22 * w - 0.77$
Suburb	$f = 0.34 * w^2 - 0.45 * w - 0.42$	$f = -0.23 * w^2 + 0.30 * w - 0.86$
Rural area	$f = 0.16 * w^2 - 0.26 * w - 0.44$	$f = -0.33 * w^2 + 0.61 * w - 1.16$

Beijing have respectively increased by  $3.05 \text{ W m}^{-2}$ ,  $0.26^\circ\text{C}$ , and  $0.25^\circ\text{C}$  (Figures 13a, 13c, and 13d, respectively). The increased heat flux occurred significantly in the six ring roads of Beijing, and the changed sensible heat flux up to  $15.21 \text{ W m}^{-2}$ , the ground temperature and 2-m temperature increased  $0.99^\circ\text{C}$  and  $0.81^\circ\text{C}$ , respectively. Also, the net infrared radiation and absorbed solar radiation increased by about 4.4 and  $0.25 \text{ W m}^{-2}$  in the city center (Figures 13f and 13g, respectively). Correspondingly, the heat flux to soil also increased (Figure 13h, where downward is positive). In addition, the increased heat flux also increased the amount of kinetic energy in the boundary layer, which in turn increased the wind speed (Figure 13e). The above results indicate that the release of anthropogenic heat can increase the urban canopy temperature and increase the amount of heat transferred to the ground.

### 3.4.5. Effects of Urban Water Planning Implementation

CAS-LSM includes urban water planning, which can be used for urban water management. We first investigated the cooling effects of different urban water usages. In the simulations, road sprinkling was mainly carried out at night to avoid interference with traffic. Figure S3 shows that road sprinkling decreased the temperature by about  $0.5\text{--}1^\circ\text{C}$  in the city center, while in rural areas, the temperature did not decrease significantly. Figure S4 shows that the temperature decreased by more than  $1^\circ\text{C}$  in the city center due to urban irrigation. In rural areas, the cooling effect of irrigation lasted from day to night. This is due to water evaporation from farm crops after daytime irrigation, and the cooling effect continued at nighttime. This effect was much more pronounced in rural areas than in the city center and suburbs. Generally, the cooling effect of urban irrigation was stronger than that of road sprinkling due to more water being used in the former.

To obtain the optimal water-use scheme, we first fitted the relationship between the amount of water used and the subsequent cooling effect (Table 5). The normalized quantities of water used for road sprinkling in the city center, suburbs, and rural areas were  $0.528 \times 10^8$ ,  $0.2868 \times 10^8$ , and  $0.039 \times 10^8 \text{ m}^3 \text{ month}^{-1}$ , respectively. For urban irrigation, we found values of  $0.81 \times 10^8$ ,  $1.72 \times 10^8$ , and  $4.45 \times 10^8 \text{ m}^3 \text{ month}^{-1}$ , respectively. In the simulations, we used constraint conditions based on the Water Resources Bulletin of Beijing, Quality Standards for Road Cleaning (NO: DB11/T 353-2006) and the text entitled “Water Supply Engineering,” (Table 6). Moreover, based on Beijing’s 13th Five-Year Plan, the water supply in Beijing, and the total amount of water used for road sprinkling and urban irrigation was set to  $43 \times 10^8$  and  $17 \times 10^8 \text{ m}^3 \text{ yr}^{-1}$ , respectively. The Optimization Toolbox in MATLAB was used to calculate the results, which show that the quantities of water used for road sprinkling in the city center, suburbs and the rural areas were  $0.21 \times 10^8$ ,  $0.06 \times 10^8$ , and  $0.04 \times 10^7 \text{ m}^3 \text{ month}^{-1}$  (the normalized amounts were 0.4, 0.2, and 0.1, respectively) and the amounts of water used for urban irrigation in the city center, suburbs, and the rural areas were  $0.35 \times 10^8$ ,  $0.62 \times 10^8$ , and  $1.78 \times 10^8 \text{ m}^3 \text{ month}^{-1}$  (the normalized amounts were 0.43, 0.36, and 0.40, respectively). In general, 90% of the total water supply should be used for urban irrigation to obtain greater cooling effects, which could potentially yield a temperature decrease of  $1.9^\circ\text{C}$ .

**Table 6***Constraint Conditions on Water Usage in Urban, Suburban, and Rural Areas*

	RS urban	RS suburb	RS rural	UI urban	UI suburb	UI rural
Units ( $10^8 \text{ m}^3 \text{ month}^{-1}$ )	0.528	0.2868	0.039	0.81	1.72	4.45
The lowest water demand	0.4	0.2	0.1	0.1	0.1	0.1
The highest water supply	1	1	1	2	2	2

Note. RS means road sprinkling, and UI means urban irrigation.

#### 4. Conclusions and Discussion

In the present study, we developed a LSM, CAS-LSM, which considers human water regulation, ground-water lateral flow, the movement of frost and thaw fronts, riverine-dissolved inorganic nitrogen transport, anthropologic heat release, urban water usage, and urban planning. We conducted global simulations using the developed model to evaluate its performance. Compared with local and global data sets, it was shown that CAS-LSM has a good ability to reproduce ecohydrological processes.

The simulated results illustrated the effects of human activities on hydrological and ecological processes. Groundwater lateral flow played a critical role in offsetting depression cones caused by intensive ground-water pumping. The offset rate increased as the aquifer thickness increased and up to 40%. Permafrost and seasonally frozen areas were easily distinguished. Global warming dominated the degradation of permafrost, where the maximum thaw depth increased at a rate of  $3.62 \text{ mm yr}^{-1}$  in permafrost areas. In the seasonally frozen areas, the maximum soil frost depth decreased at a rate of  $1.26 \text{ mm yr}^{-1}$  within natural areas and decreased by  $1.89 \text{ mm yr}^{-1}$  in human-dominated areas. Nitrogen fertilizer application increased the riverine dissolved inorganic nitrogen flow rates, especially in the central United States (the Mississippi River), western Europe, and northern China (the Yellow River and the Yangtze River).

We also conducted simulations over Beijing using the WRF model coupled with CAS-LSM to verify the model's ability to simulate the effects of urban planning implementation. The results showed that anthropogenic heat release enhanced the sensible heat flux and the temperature in the city center. The cooling effect of urban irrigation was stronger than that of road sprinkling, and it was suggested that most of total water supply in Beijing should be used for urban irrigation to obtain a greater cooling effect.

Overall, the results found here suggest that CAS-LSM is an effective tool for studying the effects of human activities on land surface processes. More comprehensive representations of physical and human-activity processes will contribute to the development of the climate system model, and we will present more detailed results of the interactions between human activities and climate in future work.

#### Data Availability Statement

The source codes of CAS-LSM could be obtained after filling out the related memorandum ([http://www.lasg.ac.cn/news/202004/t20200425\\_553389.html](http://www.lasg.ac.cn/news/202004/t20200425_553389.html)). The global elevation and land cover data sets are accessible online (<https://globalmaps.github.io>). The fertilizer use data were obtained online (<https://doi.pangaea.de/10.1594/PANGAEA.863323>). The point-source pollution data were obtained online (<https://easy.dans.knaw.nl/ui/datasets/id/easy-dataset:64145>). The GRACE satellite data for the terrestrial water storage are accessible online (<https://podaac.jpl.nasa.gov/datasetlist?search=GRACE>). The groundwater table depth observations are available online ([https://glowasis.deltares.nl/thredds/catalog/opendap/opendap/Equilibrium\\_Water\\_Table/catalog.html](https://glowasis.deltares.nl/thredds/catalog/opendap/opendap/Equilibrium_Water_Table/catalog.html)). The ESA-CCI soil moisture data set was downloaded online (<https://www.esa-soilmoisture-cci.org/node/145>). The FLUXNET-MTE product is available online (<https://www.bgc-jena.mpg.de/geodb/projects/FileDetails.php>).

#### Acknowledgments

This work was jointly supported by the National Natural Science Foundation of China (Grant 41830967), the National Key R&D Program of China (2018YFC1506602), and the Key Research Program of Frontier Sciences, CAS (QYZDY-SSW-DQC012).

#### References

- Bear, J. (1972). *Dynamics of fluids in porous Media* (pp. 361–373). New York: American Elsevier.
- Block, A., Keuler, K., & Schaller, E. (2004). Impacts of anthropogenic heat on regional climate patterns. *Geophysical Research Letters*, 31, L12211. <https://doi.org/10.1029/2004gl019852>
- Bouwman, A. F., Beusen, A., Overbeek, C., Bureau, D., Pawłowski, M., & Glibert, P. (2013). Hindcasts and future projections of global inland and coastal nitrogen and phosphorus loads due to finfish aquaculture. *Reviews in Fisheries Science*, 21, 112–156. <https://doi.org/10.1080/10641262.2013.790340>
- Brown, J., Ferrians, O. J. Jr., Heginbottom, J. A., & Melnikov, E. S. (1997). Circum-Arctic map of permafrost and ground-ice conditions. U.S. Geol. Surv. in Cooperation with the Circum-Pacific Council for Energy and Mineral Resources, Circum-Pacific Map Series CP-45, scale 1:10,000,000, 1 sheet.
- Chen, M. X., Zhang, H., Liu, W. D., & Zhang, W. Z. (2014). The global pattern of urbanization and economic growth: Evidence from the last three decades. *PLoS ONE*, 9, e103799. <https://doi.org/10.1371/journal.pone.0103799>
- Dai, Y., Zeng, X., Dickinson, R. E., Baker, I., Bonan, G. B., Bosilovich, M. G., et al. (2003). The common land model. *Bulletin of the American Meteorological Society*, 84(8), 1013–1023. <https://doi.org/10.1175/BAMS-84-8-1013>
- Di, Z. H., Xie, Z. H., Yuan, X., Tian, X. J., Luo, Z. D., & Chen, Y. N. (2011). Prediction of water table depths under soil water-groundwater interaction and stream water conveyance. *Science China Earth Sciences*, 54, 420–430. <https://doi.org/10.1007/s11430-010-4050-8>
- Dorigo, W. A., Wagner, W., Albergel, C., Albrecht, F., Balsamo, G., Brocca, L., et al. (2017). ESA CCI soil moisture for improved Earth system understanding: State-of-the art and future directions. *Remote Sensing of Environment*, 203, 185–215. <https://doi.org/10.1016/j.rse.2017.07.001>

- Drech, G. V., Bouwman, A. F., Knoop, J. M., Beusen, A. H. W., & Meinardi, C. R. (2003). Global modeling of the fate of nitrogen from point and nonpoint sources in soils, groundwater, and surface water. *Global Biogeochemical Cycles*, 17, 1115. <https://doi.org/10.1029/2003GB002060>
- Fan, Y. (2015). Groundwater in the Earth's critical zone: Relevance to large-scale patterns and processes. *Water Resources Research*, 51, 3052–3069. <https://doi.org/10.1002/2015WR017037>
- Fan, Y., Li, H., & Miguez-Macho, G. (2013). Global patterns of groundwater table depth. *Science*, 339, 940–943. <https://doi.org/10.1126/science.1229881>
- Friedl, M. A., McIver, D. K., Hodges, J. C., Zhang, X., Muchoney, D., Strahler, A. H., et al. (2002). Global land cover mapping from MODIS: Algorithms and early results. *Remote Sensing of Environment*, 83(1–2), 287–302. [https://doi.org/10.1016/S0034-4257\(02\)00078-0](https://doi.org/10.1016/S0034-4257(02)00078-0)
- Gao, J., Xie, Z., Wang, A., Liu, S., Zeng, Y., Liu, B., et al. (2019). A new frozen soil parameterization including frost and thaw fronts in the Community Land Model. *Journal of Advances in Modeling Earth Systems*, 11, 659–679. <https://doi.org/10.1029/2018MS001399>
- Gao, J., Xie, Z., Wang, A., & Luo, Z. (2016). Numerical simulation based on two-directional freeze and thaw algorithm for thermal diffusion model. *Applied Mathematics and Mechanics*, 37, 1467–1478. <https://doi.org/10.1007/s10483-016-2106-8>
- Gent, P. R., Danabasoglu, G., Donner, L. J., Holland, M. M., Hunke, E. C., Jayne, S. R., et al. (2011). The community climate system model version 4. *Journal of Climate*, 24(19), 4973–4991. <https://doi.org/10.1175/2011JCLI4083.1>
- Gleeson, T., Moosdorf, N., Hartmann, J., & Beek, L. (2014). A glimpse beneath Earth's surface: GLobal HYdrogeology MaPS (GLHYMPS) of permeability and porosity. *Geophysical Research Letters*, 41, 3891–3898. <https://doi.org/10.1002/2014GL059856>
- Gleeson, T., Smith, L., Moosdorf, N., Hartmann, J., Dürr, H. H., Manning, A. H., et al. (2011). Mapping permeability over the surface of the Earth. *Geophysical Research Letters*, 38, L02401. <https://doi.org/10.1029/2010GL045565>
- Graham, S. T., Famiglietti, J. S., & Maidment, D. R. (1999). Five-minute, 1/2°, and 1° data sets of continental watersheds and river networks for use in regional and global hydrologic and climate system modeling studies. *Water Resources Research*, 35, 583–587. <https://doi.org/10.1029/1998WR900068>
- Grimmond, C. S. B. (1992). The suburban energy balance: Methodological considerations and results for a mid-latitude west coast city under winter and spring conditions. *International Journal of Climatology*, 12(5), 481–497. <https://doi.org/10.1002/joc.3370120506>
- Gruber, A., Dorigo, W. A., Crow, W., & Wagner, W. (2017). Triple collocation-based merging of satellite soil moisture retrievals. *IEEE Transactions on Geoscience and Remote Sensing*, 55, 1–13. <https://doi.org/10.1109/TGRS.2017.2734070>
- Gruber, A., Scanlon, T., van der Schalie, R., Wagner, W., & Dorigo, W. (2019). Evolution of the CCI soil moisture climate data records and their underlying merging methodology. *Earth System Science Data*, 11, 717–739. <https://doi.org/10.5194/essd-11-717-2019>
- Harada, Y., Tsuchiya, F., Takeda, K., & Muneoka, T. (2009). Characteristics of ground freezing and thawing under snow cover based on longterm observation. *Seppyo*, 71, 241–252. [https://doi.org/10.1175/Bams-D-12-0012.1](https://doi.org/10.14851/jcsir.2009.0.57.0</a></p><p>Hurrell, J. W., Holland, M. M., Gent, P. R., Ghan, S., Kay, J. E., Kushner, P. J., et al. (2013). The community earth system model a framework for collaborative research. <i>Bulletin of the American Meteorological Society</i>, 94, 1339–1360. <a href=)
- Iwata, Y., Hayashi, M., Suzuki, S., Hirota, T., & Hasegawa, S. (2010). Effects of snow cover on soil freezing, water movement, and snowmelt infiltration: A paired plot experiment. *Water Resources Research*, 46, W09504. <https://doi.org/10.1029/2009WR008070>
- Ji, P., Yuan, X., & Liang, X.-Z. (2017). Do lateral flows matter for the hyperresolution land surface modeling? *Journal of Geophysical Research: Atmospheres*, 122, 12,077–12,092. <https://doi.org/10.1002/2017JD027366>
- Jumikis, A. R. (1977). *Thermal geotechnics* (p. 375). New Brunswick, NJ: Rutgers University Press.
- Jung, M., Koitala, S., Weber, U., Ichii, K., Gans, F., Camps-Valls, G., et al. (2019). The FLUXCOM ensemble of global land-atmosphere energy fluxes. *Scientific data*, 6, 74. <https://doi.org/10.1038/s41597-019-0076-8>
- Jung, M., Reichstein, M., Margolis, H. A., Cescatti, A., Richardson, A. D., Arai, M. A., et al. (2011). Global patterns of land-atmosphere fluxes of carbon dioxide, latent heat, and sensible heat derived from eddy covariance, satellite, and meteorological observations. *Journal of Geophysical Research*, 116, G00J07. <https://doi.org/10.1029/2010JG001566>
- Kowalczyk, E. A., Stevens, L., Law, R. M., Dix, M., Wang, Y. P., Harman, I. N., et al. (2013). The land surface model component of ACCESS: Description and impact on the simulated surface climatology. *Australian Meteorological and Oceanographic Journal*, 63, 65–82. <https://doi.org/10.22499/2.6301.005>
- Lawrence, D. M., Fisher, R. A., Koven, C. D., Oleson, K. W., Swenson, S. C., Bonan, G., et al. (2019). The Community Land Model version 5: Description of new features, benchmarking, and impact of forcing uncertainty. *Journal of Advances in Modeling Earth Systems*, 11, 4245–4287. <https://doi.org/10.1029/2018MS001583>
- Lawrence, D. M., Oleson, K. W., Flanner, M. G., Thornton, P. E., Swenson, S. C., Lawrence, P. J., et al. (2011). Parameterization improvements and functional and structural advances in version 4 of the Community Land Model. *Journal of Advances in Modeling Earth Systems*, 3, M03001. <https://doi.org/10.1029/2011MS000045>
- Li, L. J., Yu, Y. Q., Tang, Y. L., Lin, P. F., Xie, J. B., Song, M. R., et al. (2020). The Flexible Global Ocean–Atmosphere–Land System Model Grid-Point Version 3 (FOGALS-g3): Description and evaluation. *Journal of Advances in Modeling Earth Systems*, 12, e2019MS002012. <https://doi.org/10.1029/2019MS002012>
- Liang, X., & Xie, Z. (2003). Important factors in land–atmosphere interactions: Surface runoff generations and interactions between surface and groundwater. *Global and Planetary Change*, 38(1–2), 101–114. [https://doi.org/10.1016/S0921-8181\(03\)00012-2](https://doi.org/10.1016/S0921-8181(03)00012-2)
- Liu, B. (2019). *Land surface model considering urban planning and coupling with regional climate model*, (doctoral dissertation). Retrieved from Chinese Science Citation Database. Beijing, China: University of Chinese Academy of Sciences. <https://dpaper.webvpn.las.ac.cn> (in Chinese)
- Liu, S., Xie, Z., Zeng, Y., Liu, B., Li, R., Wang, Y., et al. (2019). Effects of anthropogenic nitrogen discharge on dissolved inorganic nitrogen transport in global rivers. *Global Change Biology*, 25, 1493–1513. <https://doi.org/10.1111/gcb.14570>
- Maxwell, R., Condon, L., & Kollet, S. (2015). A high-resolution simulation of groundwater and surface water over most of the continental US with the integrated hydrologic model ParFlow v3. *Geoscientific Model Development*, 8, 923–937. <https://doi.org/10.5194/gmd-8-923-2015>
- Maxwell, R. M., & Condon, L. E. (2016). Connections between groundwater flow and transpiration partitioning. *Science*, 353, 377–380. <https://doi.org/10.1126/science.aaf7891>
- Miliaresis, G. C., & Argialas, D. (1999). Segmentation of physiographic features from the global digital elevation model/GTOPO30. *Computers & Geosciences*, 25(7), 715–728. [https://doi.org/10.1016/S0098-3004\(99\)00025-4](https://doi.org/10.1016/S0098-3004(99)00025-4)
- Miliaresis, G. C., & Argialas, D. (2002). Quantitative representation of mountain objects extracted from the global digital elevation model (GTOPO30). *International Journal of Remote Sensing*, 23(5), 949–964. <https://doi.org/10.1080/01431160110070690>

- Morée, A., Beusen, A., Bouwman, A., & Willems, W. (2013). Exploring global nitrogen and phosphorus flows in urban wastes during the twentieth century. *Global Biogeochemical Cycles*, 27, 836–846. <https://doi.org/10.1002/gbc.20072>
- Niu, G.-Y., Yang, Z.-L., Mitchell, K. E., Chen, F., Ek, M. B., Barlage, M., et al. (2011). The community Noah land surface model with multiparameterization options (Noah-MP): 1. Model description and evaluation with local-scale measurements. *Journal of Geophysical Research*, 116, D12109. <https://doi.org/10.1029/2010JD015139>
- Oleson, K. (2013). Technical description of version 4.5 of the Community Land Model (CLM), Natl. Cent. for Atmos., Res., Tech. Note NCAR/TN-503+ STR.
- Pang, Q., Cheng, G., Li, S., & Zhang, W. (2009). Active layer thickness calculation over the Qinghai–Tibet Plateau. *Cold Regions Science and Technology*, 57(1), 23–28. <https://doi.org/10.1016/j.coldregions.2009.01.005>
- Pokhrel, Y. N., Koitala, S., Yeh, P. J. F., Hanasaki, N., Longuevergne, L., Kanae, S., & Oki, T. (2015). Incorporation of groundwater pumping in a global land surface model with the representation of human impacts. *Water Resources Research*, 51, 78–96. <https://doi.org/10.1002/2014WR015602>
- Rizvi, S. H., Alam, K., & Iqbal, M. J. (2019). Spatio-temporal variations in urban heat island and its interaction with heat wave. *Journal of Atmospheric and Solar-Terrestrial Physics*, 185, 50–57. <https://doi.org/10.1016/j.jastp.2019.02.001>
- Rodell, M., Velicogna, I., & Famiglietti, J. S. (2009). Satellite-based estimates of groundwater depletion in India. *Nature*, 460(7258), 999–1002. <https://doi.org/10.1038/nature08238>
- Sailor, D. J. (2011). A review of methods for estimating anthropogenic heat and moisture emissions in the urban environment. *International Journal of Climatology*, 31(2), 189–199. <https://doi.org/10.1002/joc.2106>
- Sailor, D. J., & Lu, L. (2004). A top-down methodology for developing diurnal and seasonal anthropogenic heating profiles for urban areas. *Atmospheric Environment*, 38(17), 2737–2748. <https://doi.org/10.1016/j.atmosenv.2004.01.034>
- Schuur, E. A., Vogel, J. G., Crummer, K. G., Lee, H., Sickman, J. O., & Osterkamp, T. (2009). The effect of permafrost thaw on old carbon release and net carbon exchange from tundra. *Nature*, 459(7246), 556–559. <https://doi.org/10.1038/nature08031>
- Shangguan, W., Hengl, T., Mendes de Jesus, J., Yuan, H., & Dai, Y. (2017). Mapping the global depth to bedrock for land surface modeling. *Journal of Advances in Modeling Earth Systems*, 9, 65–88. <https://doi.org/10.1002/2016MS000686>
- Siebert, S., Döll, P., Hoogeveen, J., Faures, J.-M., Frenken, K., & Feick, S. (2005). Development and validation of the Global Map of Irrigation Areas. *Hydrology and Earth System Sciences*, 9, 535–547. <https://doi.org/10.5194/hess-9-535-2005>
- Seitzinger, S., Harrison, J., Dumont, E., Beusen, A. H., & Bouwman, A. (2005). Sources and delivery of carbon, nitrogen, and phosphorus to the coastal zone: An overview of Global Nutrient Export from Watersheds (NEWS) models and their application. *Global Biogeochemical Cycles*, 19, GB4S01. <https://doi.org/10.1029/2005GB002606>
- Tapley, B. D., Bettadpur, S., Watkins, M., & Reigber, C. (2004). The gravity recovery and climate experiment: Mission overview and early results. *Geophysical Research Letters*, 31, L09607. <https://doi.org/10.1029/2004GL019920>
- Tateishi, R., Uriyangqai, B., Al-Bilbisi, H., Ghar, M. A., Tsendl-Ayush, J., Kobayashi, T., et al. (2011). Production of global land cover data—GLCNMO. *International Journal of Digital Earth*, 4(1), 22–49. <https://doi.org/10.1080/17538941003777521>
- Tian, Y., Zheng, Y., & Zheng, C. (2016). Development of a visualization tool for integrated surface water–groundwater modeling. *Computational Geosciences*, 86, 1–14. <https://doi.org/10.1016/j.cageo.2015.09.019>
- Tiwari, V. M., Wahr, J., & Swenson, S. (2009). Dwindling groundwater resources in northern India, from satellite gravity observations. *Geophysical Research Letters*, 36, L18401. <https://doi.org/10.1029/2009GL039401>
- Tramontana, G., Jung, M., Schwalm, C. R., Ichii, K., Camps-Valls, G., Ráduly, B., et al. (2016). Predicting carbon dioxide and energy fluxes across global FLUXNET sites with regression algorithms. *Biogeosciences*, 13, 4291–4313. <https://doi.org/10.5194/bg-13-4291-2016>
- Viovy, N. (2011). CRUNCEP dataset. Available at: [ftp://nacp.ornl.gov/synthesis/2009/frescati/temp/land\\_use\\_change/original/readme.htm](ftp://nacp.ornl.gov/synthesis/2009/frescati/temp/land_use_change/original/readme.htm)
- Wang, L., Xie, Z., Xie, J., Zeng, Y., Liu, S., Jia, B., et al. (2020). Implementation of groundwater lateral flow and human water regulation in CAS-FGOALS-g3. *Journal of Geophysical Research: Atmospheres*, 125, e2019JD032289. <https://doi.org/10.1029/2019JD032289>
- Wang, Y., Xie, Z., Jia, B., Wang, L., Li, R., Liu, B., et al. (2020). Sensitivity of snow simulations to different atmospheric forcing data sets in the land surface model CAS-LSM. *Journal of Geophysical Research: Atmospheres*, 125, e2019JD032001. <https://doi.org/10.1029/2019JD032001>
- Wang, Y., Xie, Z., Liu, S., Wang, L., Li, R., Chen, S., et al. (2020). Effects of anthropogenic disturbances and climate change on riverine dissolved inorganic nitrogen transport. *Journal of Advances in Modeling Earth Systems*, 12, e2020MS002234. <https://doi.org/10.1029/2020MS002234>
- Washington, W. M. (1972). Numerical climatic-change experiments: The effect of man's production of thermal energy. *Journal of Applied Meteorology*, 11(5), 768–772. [https://doi.org/10.1175/1520-0450\(1972\)011Z.0.CO;2](https://doi.org/10.1175/1520-0450(1972)011Z.0.CO;2)
- Wood, E. F., Roundy, J. K., Troy, T. J., Van Beek, L., Bierkens, M. F., Blyth, E., et al. (2011). Hyperresolution global land surface modeling: Meeting a grand challenge for monitoring Earth's terrestrial water. *Water Resources Research*, 47, W05301. <https://doi.org/10.1029/2010WR010090>
- Xia, J., McGuire, A. D., Lawrence, D., Burke, E., Chen, G., Chen, X., et al. (2017). Terrestrial ecosystem model performance in simulating productivity and its vulnerability to climate change in the northern permafrost region. *Journal of Geophysical Research: Biogeosciences*, 122, 430–446. <https://doi.org/10.1002/2016JG003384>
- Xie, Z., Liu, S., Zeng, Y., Gao, J., Qin, P., Jia, B., et al. (2018). A high-resolution land model with groundwater lateral flow, water use, and soil freeze-thaw front dynamics and its applications in an endorheic basin. *Journal of Geophysical Research: Atmospheres*, 123, 7204–7222. <https://doi.org/10.1029/2018JD028369>
- Xie, Z., Wang, L., Jia, B., & Yuan, X. (2016). Measuring and modeling the impact of a severe drought on terrestrial ecosystem CO<sub>2</sub> and water fluxes in a subtropical forest. *Journal of Geophysical Research: Biogeosciences*, 121, 2576–2587. <https://doi.org/10.1002/2016JG003437>
- Xie, C., & William, A. (2013). A simple thaw-freeze algorithm for a multi-layered soil using the Stefan equation. *Permafrost and Periglacial Processes*, 24(3), 252–260. <https://doi.org/10.1002/ppp.1770>
- Yi, S., Arain, M. A., & Woo, M. K. (2006). Modifications of a land surface scheme for improved simulation of ground freeze-thaw in northern environments. *Geophysical Research Letters*, 33, L13501. <https://doi.org/10.1029/2006GL026340>
- Zeng, Y., Xie, Z., & Liu, S. (2017). Seasonal effects of irrigation on land-atmosphere latent heat, sensible heat, and carbon fluxes in semiarid basin. *Earth System Dynamics*, 8, 113. <https://doi.org/10.5194/ESD-8-113-2017>
- Zeng, Y., Xie, Z., Liu, S., Xie, J., Jia, B., Qin, P., & Gao, J. (2018). Global land surface modeling including lateral groundwater flow. *Journal of Advances in Modeling Earth Systems*, 10, 1882–1900. <https://doi.org/10.1029/2018MS001304>

- Zeng, Y., Xie, Z., Yu, Y., Liu, S., Wang, L., Jia, B., et al. (2016). Ecohydrological effects of stream–aquifer water interaction: A case study of the Heihe River Basin, northwestern China. *Hydrology and Earth System Sciences*, 20, 2333–2352. <https://doi.org/10.5194/hess-20-2333-2016>
- Zeng, Y., Xie, Z., Yu, Y., Liu, S., Wang, L., Zou, J., et al. (2016). Effects of anthropogenic water regulation and groundwater lateral flow on land processes. *Journal of Advances in Modeling Earth Systems*, 8, 1106–1131. <https://doi.org/10.1002/2016MS000646>
- Zeng, Y., Xie, Z., & Zou, J. (2017). Hydrologic and climatic responses to global anthropogenic groundwater extraction. *Journal of Climate*, 30, 71–90. <https://doi.org/10.1175/jcli-d-16-0209.1>
- Zhao, L., Oppenheimer, M., Zhu, Q., Baldwin, J. W., Ebi, K. L., Bou-Zeid, E., et al. (2018). Interactions between urban heat islands and heat waves. *Environmental Research Letters*, 13, 034003. <https://doi.org/10.1088/1748-9326/aa9f73>
- Zou, J., Xie, Z., Yu, Y., Zhan, C., & Sun, Q. (2014). Climatic responses to anthropogenic groundwater exploitation: A case study of the Haihe River Basin, northern China. *Climate Dynamics*, 42, 2125–2145. <https://doi.org/10.1007/s00382-013-1995-2>